Stereospecific Collision-Induced Dissociation and Vibrational Spectroscopy of Protonated Cyclo (Tyr-Pro)

Ariel Pérez-Mellor, Ivan Alata, Valeria Lepere, Riccardo Spezia, Anne Zehnacker-Rentien

Stereospecific Collision-Induced Dissociation and Vibrational Spectroscopy of Protonated Cyclo (Tyr-Pro)

Ariel Pérez-Mellor,[a)b)] Ivan Alata,[a)] Valeria Lepere,[a)] Riccardo Spezia,[b)] and Anne Zehnacker-Rentien [a)*1]

a) Université Paris-Saclay, CNRS, Institut des Sciences Moléculaires d'Orsay, 91405, Orsay, France

b) Laboratoire de Chimie Théorique, Sorbonne Université, UMR 7616 CNRS, 4, Place Jussieu, 75005 Paris, France.

Abstract

The protonated cyclo (LTyr-LPro) and cyclo (LTyr-DPro) dipeptides based on a diketopiperazine (DKP) ring are studied by tandem mass spectrometry in a Fourier transform ion cyclotron resonance (FT-ICR) mass spectrometer. Collision-induced dissociation (CID) and infrared multiple-photon dissociation (IRMPD) spectroscopy results are interpreted with the aid of quantum chemical calculations and chemical dynamics simulations. All the conformers identified for each diastereomer, denoted c-LLH$^+$ and c-LDH$^+$, respectively, are protonated on the carbonyl group of the tyrosine. The most stable form has an extended structure with the aromatic ring oriented outside the DKP ring; it is stabilized by an OH$^+$…π interaction. Distinct IR signatures are obtained for the extended conformers of c-LLH$^+$ and c-LDH$^+$, which differ by the strength of the OH$^+$…π interaction, much stronger in c-LLH$^+$. Less stable species with the aromatic ring folded over the DKP ring are kinetically trapped in our experimental conditions, but their IR spectrum is identical for c-LLH$^+$ and c-LDH$^+$. The main collision-induced dissociation products of the protonated dipeptides are analyzed using chemical dynamics simulations. More efficient CID is observed for c-LDH$^+$, in particular for the formation of the iminium ion of tyrosine. In contrast to the monomers, the protonated dimers of c-LLH$^+$ and c-LDH$^+$ show identical IR spectra. This is explained in terms of a structure involving a single strong OH$^+$…O interaction between subunits not sensitive to the absolute configuration of the residues, *i.e.*, from a folded protonated monomer to an extended neutral monomer.

[1] anne.zehnacker-rentien@universite-paris-saclay.fr

Introduction

The shape of biopolymers like peptides and proteins is controlled by non-covalent interactions, among which hydrogen bonds play a major role.[1] The study of short peptide chains in the gas phase, isolated from any substrate or solvent, helps to understand the nature of these intramolecular non-covalent interactions, which in turn influence the folding propensity of peptides and proteins to well-defined secondary structures, such as helices or turns. The conformational landscape of isolated neutral peptides,[2-4] including cyclic peptides,[5-8] has been the subject of numerous studies. Protonated peptides have also been extensively studied by mass spectrometry coupled to laser fragmentation spectroscopy, either in the IR or in the UV range.[9-17] In addition to optical spectroscopy measurements, important structural information on the amino-acid sequence and the secondary structure is gained from the analysis of the collision-induced dissociation (CID) or electron-capture dissociation (ECD) fragments,[18-28] in particular for assessing the influence of stereochemical aspects on the structures.[29]

Among the factors structuring the supramolecular shape of peptides in a well-defined and orderly manner, the absolute configuration of the sub-units plays an important role. Although extensive work has been devoted to charged chiral molecules or clusters isolated in the gas phase,[30-44] studies of the role of the residue's chirality on the structure and reactivity of peptides are still scarce. The influence of the residues chirality on a neutral peptide structure has been studied for α-peptides like Val-Phe and Phe-Phe[8, 45] or capped Phe-Ala[46] and Phe-Phe,[47] and for artificial β- or γ-peptides.[6, 48, 49] As per charged species, ion mobility experiments show that the presence of a single amino acid in an alanine polymer is indeed enough for disrupting its regular and ordered α-helix.[50] Replacing a single Tyr residue by its enantiomer in the Trp cage protein induces modifications detectable by ECD.[51] Vibrational laser spectroscopy coupled to mass spectrometry evidences different structures for protonated di- and tetra-phenylalanine depending on the absolute configuration of the residue.[52, 53] Diastereomers peptides may also have different proton affinities.[54] Fragmentation efficiency may be different, or not, for peptides containing residues of identical or opposite absolute configurations. For example, ECD results are identical for the copper complexes with the cyclic DHis-βAla-LHis-LLys and all-LHis-βAla-His-Lys peptides.[55] In contrast, fragmentation of copper complexes of diastereomer pentapeptides leads to stereospecific fragments intensities.[56]

We have recently examined the influence of chirality on the structure of cyclic dipeptides containing a diketopiperazine (DKP) ring. They constitute an important class of biomolecules due to potential anticancer or antiviral properties,[57, 58] Only a few gas-phase structural studies of DKP peptides have been reported so far.[5, 8, 59-63] The existence of DKP *vs.* oxazolone structures as CID products of polypeptides has been widely discussed.[64-67] Early IRMPD experiments have characterized the nature of the b_2 fragments of protonated Ala-Ala-Gly or Ala_3; they unambiguously show that it is an oxazolone structure.[68, 69] For larger peptides, IRMPD results and DFT calculations also suggest that the oxazolone structure is the most stable b_n fragment.[70] The CID mechanism of DKPs has been also studied, to infer whether fragmentation directly occurs from the most stable O-protonated species or if proton transfer to the amide nitrogen comes first.[71] This mechanism has also been tackled from a theoretical point of view by means of chemical dynamics simulations.[72]

From the structural point of view, the DKP ring imposes rigidity to the system. The conformation of the peptide ring is planar for cyclo (Gly-Gly)[73] but becomes out of plane for bulky substituents. The orientation of the substituent, folded over the DKP ring or extended outwards, strongly depends on the nature and the absolute configuration of the residues, and the charge state.[8, 61, 74]Among the studied DKP peptides, cyclo (Tyr-Pro) stands out due to the presence of a second ring, the proline. Because proline is the only α-amino acid with a pyrrolidine ring, it induces a conformational bias resulting in structural modifications such as kinks in the α-helices or turns in the β-sheets. Its vibrational spectroscopy has been studied under matrix-isolation conditions.[75] That of protonated proline, its proton-bound dimer, and 4-hydroxyproline has been studied by infrared multiple-photon dissociation (IRMPD) under ion trap conditions.[76-78] The structure of neutral tyrosine has been widely documented under supersonic jet conditions by laser-induced fluorescence,[79] REMPI spectroscopy,[80] and UV-IR spectroscopy.[81-83] It is a highly flexible molecule, showing up to twelve conformers. Each backbone structure leads to a pair of two conformers corresponding to the aromatic OH rotamers, which cannot be distinguished by their IR spectra.[83] The conformational space of tyrosine is reduced upon protonation, and only two pairs of conformers are observed for protonated Tyrosine, which shows an interaction between NH_3^+ and the aromatic ring, or not.[12, 84-86]

Neutral cyclo (Tyr-Pro) shows two structural families under jet-cooled conditions.[5] The most stable conformation has the aromatic substituent folded over the DKP ring as it is in the solid state, and a flattened boat conformation of the DKP ring.[87] This structure is stabilized by a weak CH…π interaction. A slightly higher-energy structure is also present, with a completely

extended aromatic ring, which favors a stabilizing NH…π interaction. The influence of chirality is limited, where cyclo (LTyr–LPro) and cyclo (LTyr–DPro) only differ from each other by the strength of the CH…π and NH…π interactions.

In this work, we extend our study of neutral cyclo (Tyr-Pro)[5] to its protonated counterpart. To this end, we resort to collision-induced dissociation (CID) experiments, as well as IRMPD vibrational spectroscopy, coupled to quantum chemistry calculations of the structures and chemical dynamics simulation of the collision-induced dissociation process. The aim of this work is to assess the influence of the absolute configuration of the residues on the structure of the molecule and its dimer, and on the CID efficiency. The molecules are shown in Figure 1 and noted in short c-LLH$^+$ and c-LDH$^+$ for protonated cyclo (LTyr-LPro) and cyclo (LTyr-DPro), respectively.

Experimental and Theoretical Methods

1. Nomenclature of the Studied Systems

The numbering of the atoms is given in Figure 1 and is the same as previously introduced for neutral cyclo (Tyr-Pro).[5] We choose the Newman projection along the two $C_\alpha C_\beta$ bonds defined by Young *et al.*[88] to visualize the orientation of the tyrosine residue. The tyrosine (Y) orientation, shown in Figure 2a, is easily seen by looking through $C_\beta^5 C_\alpha^1$ while that of the proline (P) is seen by looking through $C_\beta^{14} C_\alpha^3$, see Figure 2b. Two gauche geometries, g^+ and g^-, correspond to dihedral angles τ ($NC_1C_5C_6$) of ~ 60° and ~ -60° for the L-Tyr residue, and the trans t geometry to τ ~ 180°, as shown in Figure 2a. For proline, the conformation is determined in a similar manner, by τ'($NC_3C_{14}C_{13}$). However, the proline orientation is always g^- due to the ring constraints (Figure 2b).

In protonated cyclo (Tyr-Pro), there are four main non-equivalent protonation sites, on amide oxygen or nitrogen atoms, as shown in Figure 2. They are called N-protonated for protonation of the amide nitrogen of tyrosine (N_Y^+) or proline (N_P^+) and O-protonated for protonation of the amide oxygen of tyrosine (O_Y^+) or proline (O_P^+), respectively. For the N_P^+, O_Y^+, and O_P^+ protonation sites, there are two relative positions of the proton, described by the dihedral angles $T_P^N(HC_3NH^+)$, $T_Y^O(NC_2OH^+)$, and $T_P^O(NC_4OH^+)$, respectively. A structure is said to be *cis* (C) if the dihedral angle is close to 0° and *trans* (T) when it is close to 180°. Finally, there are two orientations of the phenol hydroxyl relative to the DKP ring, type I and type II, as described for the neutral molecule and indicated in Figure 2.[5]

In what follows, we shall denote the cyclic nature of the peptide by c-, followed by the geometry g^+, g^- or t of tyrosine and g^- for that of proline. The tyrosine residue is always in its natural L configuration. When not specified otherwise, the configuration of the proline is L. D configuration is indicated in subscript. The type I or type II position of the tyrosyl OH is also indicated in the subscript. Finally, the protonation site and the proton orientation are specified in parenthesis.

2. Experimental Methods

The experimental set-up rests on the Bruker hybrid APEX, 7 T Fourier transform ion cyclotron resonance (FT-ICR) located at the mass spectrometry facility TGE ICR at the CLIO center of the Institut de Chimie Physique (Orsay). Details of the experiments can be found elsewhere and only specific parameters related to the present study are given below.[89]

Cyclo (Tyr-Pro) (99% purity – 99% enantiomeric purity) was purchased from Novopep Limited (Shanghai – China) and used without further purification. Ions were generated by electrospraying a solution of cyclo (Tyr-Pro) in a 50/50 water/methanol solvent at a low concentration (5.10^{-5} M). The electrospray ionization (ESI) conditions were as follows: flow rate of 100 μL/h, drying gas flow of 7.5 L/min, nebulizer pressure of 1.9 bar, capillary voltage of -4500 V, and drying gas temperature of 180 °C.

For recording the CID-MS^2 mass spectra of the dipeptides in the 7T FT-ICR MS, ions were first mass-selected in a quadrupole mass filter in a 0.5 Da window. The ions were then fragmented in a pressurized hexapole through multiple collisions with Ar by using a DC offset between -1 to -15 V and applying a radiofrequency (RF) voltage of variable amplitude for 300 ms. Ions were detected in the ICR cell at a background pressure of 10^{-9} mbar.

The IRMPD spectrum can be divided into two regions that correspond to two different IR light sources. The Free Electron Laser (FEL) at the Centre Laser Infrarouge d'Orsay (CLIO)[90] covers the 900-2000 cm^{-1} region while the 2400-3700 cm^{-1} region is provided by a table-top optical parametric oscillator/amplifier (OPO/OPA LaserVision). IR spectra were obtained by mass selecting the precursor ions in a 0.5 Da window, with 1s irradiation time in the 3 μm region and 2s in the fingerprint region. In both regions, a broad-band CO_2 laser (Universal Laser system, 10 W in continuous mode operation centered at λ = 10.6 μm) was synchronized with the tunable IR source to sustain the fragmentation of the ions.

The CLIO FEL[90] was operated at 25 Hz with 8 ms long bunch pulses containing 0.5-3 ps micropulses separated by 16 ns. The spectral bandwidth (full width at half-maximum FWHM) was about 10 cm^{-1} with a pulse energy of 1600 to 900 mW from 900 to 2000 cm^{-1}. The

wavelength calibration was ensured by simultaneously recording the spectrum of a polystyrene sheet and that of the studied system.

The table-top IR OPO/OPA was operated at 25 Hz with a pulse duration of 4-6 ns, spectral bandwidth 3 cm^{-1}, IR power of ~200 mW. The IR was focused at the center of the ion trap using a ZnSe lens of 400 mm focal length.

Infrared spectra were obtained by monitoring the Ln of the fragmentation efficiency $\phi = - \ln (P/(F+P))$ as a function of the IR wavelength, with F being the sum of the abundances of the fragment ions produced by IRMPD and P that of the parent ion.

3. Quantum Chemistry Calculations

The potential energy surface of cyclo (Tyr-Pro)H^+ was carefully explored, starting from all the minima found for the neutral molecule. The protonated species corresponding to these conformers were obtained by protonating either the carbonyl (O protonation) or the nitrogen (N protonation) sites. For each protonation site except the proline nitrogen, for which only one direction of the proton is possible, the two proton orientations were considered. Due to the cyclic nature of proline, its geometry was fixed, and only the six possible orientations of the phenyl substituent of tyrosine were considered. The resulting 42 conformers were optimized in the frame of the density functional theory (DFT) using the dispersion-corrected functional B3LYP-D3[91] associated with the Pople 6-311++G(d,p) split-valence basis set.[92] The B3LYP-D3 functional combines the good frequency description of the hybrid functional B3LYP[93] and inclusion of empirical dispersion corrections, which might be necessary for peptides containing an aromatic residue and to reproduce the OH…π, NH…π, and CH…π interactions. [5, 8, 53, 59, 61, 74, 91, 94, 95] The most stable structures found thereby were re-optimized at the M06-2X, using the same basis set, because this functional was shown to perform better than B3LYP for systems involving dispersion and ionic hydrogen bonds.[96] However, the relative energies of the conformers are almost identical and we shall only discuss, in what follows, the B3LYP results. The results at the M06-2X/6-311++G(d,p) level are compared with those at the B3LYP-D3 level in Tables S1 and S2 of the Supplementary Information. To reduce the computational cost, the protonated cyclo (Tyr-Pro) dimer was calculated with the same functional but the smaller 6-31+G(d,p) basis set. It was shown indeed on the example of solid-state cyclo (Phe-Phe) that the structures and vibrational frequencies are similar at the two levels of theory.[97] Different structures were constructed for the protonated dimers, containing either the most stable O-protonated or the most stable N-protonated monomer (*vide infra*) in interaction with either a CO or amide nitrogen of the neutral moiety.

The harmonic vibrational frequencies were calculated at the same level of theory as the geometry optimization. The absence of imaginary frequency was checked for all local minima found. The harmonic frequencies were scaled to account for anharmonicity and basis set incompleteness. To this end, we used the range-specific scaling factors defined for neutral cyclo (Tyr-Pro) as the slope of the linear regression of the ratio between harmonic and anharmonic frequencies for all the computed structures.[5] The scaling factor for the fingerprint, the ν(CH), and the ν(NH)/ν(OH) region is 0.977, 0.957, 0.952, respectively. Indeed, mode-dependent scaling factors based on an extensive library of systems improve agreement with the experiment.[3, 98] The vibrational spectra were simulated by convoluting the harmonic frequencies by a Lorentzian line shape (FWHM 10 cm^{-1}). All calculations were performed with the Gaussian 09 package.[99]

4. Chemical Dynamics Simulations

We have determined the structures of the fragment ions observed in the experimental CID spectra using an approach based on chemical dynamics. This approach was pioneered by Hase and co-workers[100] and recently described in an exhaustive review.[101] We only report here the technical details specific to the present work.

In this approach, we activated the fragmenting ion with excess vibrational energy. Excess energy was distributed by a microcanonical sampling of the vibrational normal modes of the studied reagent structure.[102] Due to the similitude in the CID spectra between the two diastereoisomers, only $c - g_{II}^{+}g_{D}^{-}\left(O_{Y}^{+T}\right)$ was used as the initial structure. Trajectories were propagated at seven excess energy values (367, 392, 417, 442, 467, 492, and 517 kcal/mol). Resorting to these high-energy values allowed completing the reaction despite the short simulation time, so that a qualitative assignments of the CID experiments is possible. The values were chosen to have enough fragmenting trajectories and a complete breakdown curve in the available simulation time-scale. The initial rotational energy was sampled according to the Boltzmann distribution at 300K.

The electronic structure of the systems was solved *on-the-fly* by using the RM1-D semi-empirical Hamiltonian.[103, 104] An ensemble of 5000 trajectories per excess energy was propagated by solving numerically Newton's equation of motion up to 20ps. The velocity Verlet method[105] was employed with 0.1fs time step, which ensures energy conservation within 0.20 kcal/mol. The simulations were carried out by using the chemical dynamics software VENUS[106] coupled with the MOPAC-version 5.022mn software.[107] The trajectories were then analyzed to identify fragmentation products by using an in-house code based on graph

theory.[72] This code is similar to what was done previously[108, 109] but includes the canonical labeling of the graph[110] to properly estimate the abundance of the isomers. It also involves a new method to identify the formation of ion-molecule complexes.[72] The most abundant isomers per product were then optimized at the same level of theory as the reagent.

5. Reaction rate constants calculations

The intermediate states occurring in the chemical dynamics simulations were optimized at the B3LYP/6-31G(d,p) level of theory. The transition states separating them were identified and calculated at the same level of theory using the standard procedure implemented in the Gaussian 09 software.[99] RRKM rate constants[111] were obtained based on energies and vibrational frequencies of the minima and transition states. The sum and density of states were calculated using the direct count algorithm of Beyer-Swinehart[112] with the Zhu and Hase code.[113]

Results and discussion

1. Vibrational Spectroscopy and Structure of the Monomer

1. a. IRMPD spectroscopy

The IRMPD spectra of c-LLH$^+$ and c-LDH$^+$ are shown in Figure 3. They are similar in most spectral regions but show however small differences. In the fingerprint region, the infrared spectra are recorded at two laser intensities. The spectrum recorded at high laser intensity allows observing weak bands, while that at low intensity allows avoiding saturation of the most intense transitions. A preliminary assignment of the observed bands is made based on previous results on protonated tyrosine.[12, 114] Two intense bands characterize the lower-energy region with maxima at ~1180 and ~1270 cm^{-1}, readily assigned to the phenol β(OH) and β(OH$^+$) bending modes coupled to the β(CH) bend, by comparison with protonated tyrosine. They are highlighted in pink in the spectrum of Figure 3.[114, 115] The β(NH) range, highlighted in orange, displays a band of weak intensity at 1462 cm^{-1} in c-LLH$^+$, whose counterpart is at 1466 cm^{-1} in c-LDH$^+$. The bands observed at 1507 cm^{-1} in c-LLH$^+$ and 1514 cm^{-1} in c-LDH$^+$, highlighted in purple, are the signature of the aromatic β(CH) bends of tyrosine. A weak band appears at ~1600 cm^{-1} for both diastereoisomers. The Amide I region, highlighted in beige and light purple, shows two intense bands centered at ~1697 / ~1743 cm^{-1} for c-LLH$^+$ and ~1700 / ~1748 cm^{-1} for c-LDH$^+$, typical of the ν(CN) stretch adjacent to the protonated CO and of the ν(C=O) stretch of protonated DKP rings, respectively.[61, 64] It should be mentioned that the intensity of the former substantially decreases in the spectrum recorded at low laser intensity. The peaks assigned to the ν(CO) stretch are accompanied by a shoulder on the low-energy side;

marked with a red asterisk. Finally, the higher fragmentation efficiency of c-LDH$^+$ (*vide infra*) is more visible in the low-energy range where the spectrum of c-LDH$^+$ shows saturation effects and the appearance of a new weak band at 1118 cm^{-1}, which is absent for c-LLH$^+$.

In the high-frequency region (3000-3700 cm^{-1}), the spectra are also characterized by identical features for the two diastereoisomers, notwithstanding a broad absorption centered at 3300 cm^{-1} in c-LDH$^+$ that is absent in c-LLH$^+$. For c-LLH$^+$ and c-LDH$^+$ alike, an intense band appears at ~ 3420 cm^{-1}, in a range typical of the NH stretch. An intense and narrow band takes place at 3642 cm^{-1} and it is related to the phenol OH stretch mode of the tyrosine residue.[82, 83, 86, 116] Two bands of weaker intensity appear at 3559/3596 cm^{-1} for c-LLH$^+$ and 3567/3596 cm^{-1} for c-LDH$^+$, reminiscent of the protonated ν(OH$^+$) stretch observed previously in protonated cyclo (Phe-Phe) or cyclo (Gly-Gly).[61, 64] The presence of these bands suggests that the proton is localized on one of the two carbonyl groups of the DKP ring.

1. b. Calculated structures of the monomers

The relative Gibbs free energies are summarized in Table 1 and the most stable conformers are shown in Figure 4. The calculated structures can be classified into four groups corresponding to the different protonation sites, which show very different stability. The results for type I and II conformers (see Figure 2) are identical in terms of geometries and relative Gibbs energies, within the error. Therefore, we will limit the discussion to the type II conformers. The geometric parameters of the most stable structures are listed in Table 2.

Nitrogen-protonated structures. The N-protonated structures are higher in energy by more than 10 kcal/mol than the global O-protonated minimum, as already mentioned for other protonated dipeptides.[61, 64, 71] The most stable structure protonated at the proline nitrogen, $c\text{-}g_{II}{}^{+}g^{-}\left(N_P{}^{+T}\right)$ or $c\text{-}g_{II}{}^{+}g_D{}^{-}\left(N_P{}^{+C}\right)$, is found at ΔG = 13.1 kcal/mol or 11.7 kcal/mol for c-LLH$^+$ and c-LDH$^+$, respectively. The folded g$^+$ orientation of the tyrosine residue allows an NH$^+$…π interaction between the proton on the proline nitrogen and the phenol π electron cloud. The structures with the proton on the tyrosine nitrogen are much higher (ΔG> 16 kcal/mol) in energy and will not be discussed further.

Oxygen-protonated structures. For all conformers with the proton located at the proline carbonyl, the *trans* position of the proton is more stable than the *cis* because of the steric clash between the proton and the adjacent amide hydrogen. For these structures, the most stable conformer is $c\text{-}g_{II}{}^{+}g^{-}\left(O_P{}^{+T}\right)$ for c-LLH$^+$ or $c\text{-}g_{II}{}^{+}g_D{}^{-}\left(O_P{}^{+T}\right)$ for c-LDH$^+$; it is higher in energy by 7.0 and 4.2 kcal/mol than the most stable form, respectively. In this structure, very similar for c-LLH$^+$ and c-LDH$^+$, the aromatic ring of tyrosine is folded over the DKP ring,

allowing a CH…π interaction to take place like in the neutral. The only difference between the two diastereomers is the nature of this CH…π interaction. It involves $C_{14}^{\beta}H$ for c-LLH$^+$ and $C_3^{\alpha}H$ for c-LDH$^+$. Such a difference was observed in the neutral as well as in neutral or protonated cyclo (Phe-Phe) or neutral cyclo (Tyr-Tyr).[5, 8, 59, 61, 74]

The structures protonated at the tyrosine carbonyl are the most stable of all calculated structures. In the most stable forms, namely $c\text{-}t_{II}g^-\left({O_Y}^{+T}\right)$ and $c\text{-}t_{II}{g_D}^-\left({O_Y}^{+T}\right)$, the *trans* geometry of the proton and the extended geometry of the aromatic ring (t orientation) allow a strong ionic OH$^+$….π interaction. This results in a short distance between the proton and the center of the aromatic ring, of 2.51 Å for $c\text{-}t_{II}g^-\left({O_Y}^{+T}\right)$ and 2.60 Å for $c\text{-}t_{II}{g_D}^-\left({O_Y}^{+T}\right)$. This interaction is not possible for the *cis* geometry of the proton, and the corresponding conformers are higher in energy by 5.0 kcal/mol. When the tyrosine is in g$^+$, *i.e.*, folded, as in $c\text{-}{g_{II}}^+g^-\left({O_Y}^{+T}\right)$ and $c\text{-}{g_{II}}^+{g_D}^-\left({O_Y}^{+T}\right)$, the strong OH$^+$…π interaction cannot take place, which explains the lesser stability of these structures. They are only stabilized by a CH…π interaction similar to that described before. The interaction involving $C_3^{\alpha}H$ in c-LDH$^+$ of proline is stronger than that involving $C_{14}^{\beta}H$ in c-LLH$^+$, as manifested by a shorter distance between the hydrogen and the center of the phenol group (2.50 Å compared to 2.70 Å) due to steric constraints induced by the cyclic nature of proline. For these oxygen-protonated structures at the tyrosine carbonyl, the *trans* geometry of the proton is more stable than the *cis*. Note that these folded structures are reminiscent of the most stable structures calculated for the neutral.

The most stable conformer of c-LDH$^+$ is less stable than that of c-LLH$^+$ by 0.5 kcal/mol, a point to which we shall return in the discussion. Moreover, the potential energy surface of c-LDH$^+$ seems to be shallower. In c-LLH$^+$, the main conformer involving the OH$^+$…π interaction, $c\text{-}t_{II}g^-\left({O_Y}^{+T}\right)$, is separated from the second one by 3.8 kcal/mol. In contrast, the energy difference between $c\text{-}t_{II}{g_D}^-\left({O_Y}^{+T}\right)$ and the higher-energy conformers is much smaller in c-LDH$^+$. In particular, the folded conformer protonated on tyrosine, $c\text{-}{g_{II}}^+{g_D}^-\left({O_Y}^{+T}\right)$, is expected to be populated at room temperature.

1. c. Assignment of the experimental spectra

The experimental frequencies of the ν(NH) stretch are typical of that observed for free NH in DKP peptides, which rules out the N-protonated structures. The comparison between the ν(NH) experimental band located at 3417 / 3420 cm^{-1} and the scaled ν(NH) frequency of all the calculated O-protonated conformers is shown in Figure 5. This comparison, together with the relative energies, clearly indicates that the protonation at the tyrosine CO (O_Y^+) reproduces the

experiment better than that at the proline CO (O_P^+). In particular, protonation at the O_P^+ site would perturb the free ν(NH) stretch and shift it down in frequency relative to the experiment, due to the charge delocalization on the amide bond.[61, 64]

The main features of the IRMPD spectra are interpreted by comparison with the IR spectrum of the most stable structures: $c\text{-}t_{II}g^-(O_Y{}^{+T})$, $c\text{-}g_{II}{}^+g^-(O_Y{}^{+T})$ and $c\text{-}g_{II}{}^+g^-(O_Y{}^{+C})$ for c-LLH$^+$ and $c\text{-}t_{II}g_D{}^-(O_Y{}^{+T})$, $c\text{-}g_{II}{}^+g_D{}^-(O_Y{}^{+T})$ and $c\text{-}g_{II}{}^+g_D{}^-(O_Y{}^{+C})$ for c-LDH$^+$ (Figure 3). Several bands are neither conformer nor diastereomer specific and appear in all spectra; we describe them first in what follows. The higher-energy peak at 3642 / 3643 cm^{-1} corresponds to the phenol free ν(OH) stretch of all conformers and the peak at 3417 / 3420 cm^{-1} is assigned to the ν(NH) stretch. In the Amide I and Amide II region, the band at 1743 / 1748 cm^{-1} is assigned to the free ν(C=O) stretch while that at 1697 / 1700 cm^{-1} is mainly described in terms of the protonated amide CN stretch slightly coupled to the COH$^+$ bend. Bands localized on the phenol ring are identified at 1601 / 1603 cm^{-1} and 1507 / 1514 cm^{-1} and assigned to the aromatic ν(C=C) stretch analogous to the E_{1u} vibrations in benzene (Wilson notation) and to the in-plane aromatic β(CH) bend. The broad band at 1271 / 1273 cm^{-1} is assigned to superimposed transitions assigned to modes involving β(CH) and β(OH$^+$) bending motions. Finally, the intense band at 1178 / 1183 cm^{-1} is the phenol β(OH).

The calculated spectra also show conformer-specific bands, which are described below. The bands with two maxima centered at 3559 / 3596 cm^{-1} in c-LLH$^+$ and 3567 / 3596 cm^{-1} in c-LDH$^+$ are assigned to the ν(OH$^+$) stretch of the conformers with tyrosine in g$^+$ orientation. The higher-energy peak is assigned to the ν(OH$^+$) stretch of conformers with the proton in trans position ($O_Y{}^{+T}$) while the lower-energy one is assigned to those with the proton in cis position ($O_Y{}^{+C}$). This observation leads to the conclusion that the conformers with tyrosine in g$^+$ orientation are present in our experimental conditions despite their higher relative Gibbs energy close to 5 kcal/mol in the case of c-LLH$^+$.

All bands described above are common to the two diastereomers, only shifted by a few cm^{-1}. However, some differences are experimentally visible; in particular, a broad background appears in the 3400 cm^{-1} region in c-LDH$^+$ only. The calculations suggest that the ν(OH$^+$) of $c\text{-}t_{II}g_D{}^-(O_Y{}^{+T})$ is shifted down in frequency due to the stabilizing OH$^+$…π interaction, and appears at 3410 cm^{-1}. The breadth and the red shift of the band reflect the strong interaction between OH$^+$ and the aromatic ring. We, therefore, assign the broad background observed for c-LDH$^+$ to $c\text{-}t_{II}g_D{}^-(O_Y{}^{+T})$. In the case of c-LLH$^+$, the calculations suggest that this broad band should appear at a much lower frequency (3176 cm^{-1}) for $c\text{-}t_{II}g^-(O_Y{}^{+T})$; it is therefore not

detectable experimentally due to the low intensity of the OPO in this region and to the expected breadth of the band due to the strong interaction.[117] In the Amide I region, the intense band at 1697 / 1700 cm^{-1} is assigned to the ν(CN) stretch of the protonated amide coupled to the $\delta(C_2OH^+)$ bending motion. This band presents several shoulders that can be assigned to different conformations. For the t conformers, calculations predict a band centered at 1680 / 1699 cm^{-1}. For the g^+ conformers, calculations predict transitions at 1710 / 1711 cm^{-1} for the *trans* conformers and at 1673 / 1676 cm^{-1} for the *cis*. Natural Bond Orbital (NBO) analysis was conducted to understand this difference in vibrational frequencies.[118] It comes out that delocalization from the CN orbital to the vicinal carbon atoms takes place in the cis conformers, corresponding to a stabilization of 1 kcal/mol. This effect results in a weaker CN bond hence lower frequency of the CN stretch in the cis conformers. Finally, the band at 1462 / 1446 cm^{-1} is assigned to the ν(NH) bend of the most stable conformers, $c\text{-}t_{II}g^-\left({O_Y}^{+T}\right)$ and $c\text{-}t_{II}{g_D}^-\left({O_Y}^{+T}\right)$.

The experimental spectra of the monomers are well reproduced by the calculated spectra if we consider the three most stable conformers for each diastereomer, although $c\text{-}{g_{II}}^+g^-\left({O_Y}^{+T}\right)$ and $c\text{-}{g_{II}}^+g^-\left({O_Y}^{+C}\right)$ should have negligible Boltzmann populations at room temperature. Early room-temperature or cryogenic ion trap studies of biomolecules have evidenced the trapping of several conformers that are stable in solution at room temperature.[119] Indeed, species that are stable in solution can be kinetically trapped during the ESI process, even if they are not the most stable in the gas phase.[115, 120-122] Including a continuum solvation model considerably modifies the energy ordering compared to the gas phase.[123] To test whether it could be the case for the system studied here as well, we have conducted calculations using a continuum solvation model.[124] The energy difference between the three experimentally observed c-LLH^+ conformers is reduced to 0.9 kcal/mol in aqueous solution, much smaller than in the gas phase. This decrease in relative energy is related to the fact that in water, the free protonated carbonyl of the g^+ conformers is stabilized by interacting with the solvent, in contrast with the t conformers where it is involved in the $OH^+\ldots\pi$ interaction. We should note that considering the solvent alters not only the energy order between the different conformers but also the relative stability of the diastereomers. The LDH^+ diastereomer is indeed more stable in water by 2.8 kcal/mol. This is reminiscent of the stability order observed for neutral cyclo (Tyr-Pro) in the gas phase and probably arises from the same reason. The most stable neutral conformer in the gas phase is a folded g^+ geometry like the most stable conformer of the protonated species in water, which is more stable for c-LDH^+. In chiral stationary-phase

chromatography also, changing the eluent may modify the molecular structures and the interaction mechanism so that the elution time of two enantiomers is reversed. [125]

The calculations also indicate that c-LDH$^+$ is more flexible than c-LLH$^+$. Indeed, six conformers, *i.e.*, three low-energy pairs considering the I and II orientations of the phenol OH, are predicted in the gas phase for c-LDH$^+$, with both extended and folded geometries. In contrast, only one low-energy pair is predicted for c-LLH$^+$, with an extended structure. We have already observed that protonated dipeptides or tetrapeptides of alternating absolute configuration have larger flexibility and number of calculated conformers than the corresponding all L natural polypeptides.[53]

2. Collision-Induced Dissociation and Fragmentation Simulations of the Monomer

Experimental breakdown curves of c-LLH$^+$ and c-LDH$^+$ (*m/z* 261) together with the intensity of the main CID fragment ions as a function of the collision voltage are shown in Figure 6.

The same fragments are observed for the two diastereoisomers. However, the fragmentation efficiency is slightly higher for c-LDH$^+$.

In what follows, we will qualitatively describe the channels leading to the experimentally observed fragment ions, based on the mechanisms obtained in the simulations. Chemical dynamics simulations yield all the fragmentation products experimentally observed. The ionic fragments are listed in Table 3 together with their energy obtained from the DFT static calculations performed on the product structures obtained from simulations. Figure 7 shows the most abundant isomer of the product obtained for each mass; their neutral counterparts are shown in Figure S1 of the Supplementary Information. It should be noted that these structures are the geometries obtained from simulations, *i.e.*, resulting from trajectories propagated at the ps time-scale. It is likely that some of them re-arrange after a given equilibration time, since the experiments occur on much longer time-scales, of the order of hundreds of ms.

The most intense experimental peak is due to the *m/z* 233 ($C_{13}H_{17}N_2O_2^+$) fragment, which corresponds to the loss of 28 amu from the parent, *i.e.* carbon monoxide (CO), which is common in DKP dipeptides.[126-128] This fragmentation happens at low energy, as observed in cyclo (Gly-Gly)H$^+$.[71] Chemical dynamics simulations allowed identifying two main *m/z* 233 isomeric fragments, namely, M_2 and M_3, reported in Figure 7. The former corresponds to the formation of an ion-molecule complex, already proposed for cyclo (Gly-Gly)H$^+$,[71] while the second is a linear structure that preserves the aromatic side chain as well as the proline ring.

At higher collision energy, the *m/z* 233 ion intensity starts to decrease due to the formation of secondary fragments. In particular, a weakly abundant fragment at *m/z* 205 is observed in the MS^2 spectrum of Figure 6 and corresponds to the loss of CO from *m/z* 233, resulting in $[M\text{-}CO\text{-}CO+H]^+$. This fragmentation channel is identical to that observed in cyclo (Gly-Gly)H^+ but its yield is less abundant in cyclo (Tyr-Pro)H^+.[71]

Secondary fragmentation of *m/z* 233 also results in *m/z* 188 ($C_{12}H_{14}NO^+$), which is the third more abundant channel whose ion yield constantly increases with collision energy. It results mainly from the loss of neutral formamide (NH_2CHO) from the *m/z* 233 ion. The very weak peak at *m/z* 186 ($C_{12}H_{12}NO^+$) is formed from H_2 loss from *m/z* 188.

m/z 136 ($C_8H_{10}NO^+$), whose ion yield constantly increases with collision energy, appears as the second most abundant fragment at low collision energies; it is assigned to the iminium ion of tyrosine. Its breakdown curve shows a similar energy dependence as that observed for the iminium formation from cyclo (Gly-Gly)H^+. The main calculated mechanisms consist in the formation of the $C_5ONH_8\ldots C_8H_9NO$ ion-molecule complex (structure M_2 in Figure 7) from which the iminium ion can be easily obtained *via* secondary fragmentation after proton attachment or *via* primary fragmentation of the parent ion following isomerization.

The fragments involving NH_3 loss appear at higher collision energy and correspond to channels of lesser abundance that are identified in the simulations. The *m/z* 244 ($C_{14}H_{14}NO_3^+$) peak corresponds to the loss of ammonia from the parent ion via primary fragmentation. The formation of *m/z* 216 ($C_{13}H_{14}NO_2^+$) can be obtained *via* primary fragmentation of the parent by direct loss of formamide or *via* secondary fragmentation due to ammonia loss from *m/z* 233.

Finally, the *m/z* 155 ($C_7H_{11}N_2O_2^+$) fragment does not find its counterpart in the CID spectrum of cyclo (Gly-Gly)H^+or cyclo (Ala-Ala)H^+.[71] It is also observed upon photoionization of neutral cyclo (Tyr-Pro), as a fragment of the radical cation.[5] It can be formed due to the homolytic C_α-C_β cleavage of the aromatic side-chain accompanied by hydrogen transfer from the aromatic part to the DKP ring, leading to protonated cyclo (Gly-Pro)H^+. The *m/z* 153 peak ($C_7H_9N_2O_2^+$) corresponds to the same cleavage reaction accompanied by a hydrogen transfer from the DKP ring to the aromatic side-chain.

The formation of *m/z* 154 ($C_7H_{10}N_2O_2^+$) and 107 ($C_7H_7O^+$) is also related to the C_α-C_β cleavage of the benzyl, but without additional hydrogen atom transfer. *m/z* 154 and 107 result from homolytic or heterolytic cleavage, respectively. Other fragments that contain the aromatic side-chain were identified, such as *m/z* 164 ($C_9H_{10}NO_2^+$), 147 ($C_9H_7O_2^+$), and 119 ($C_8H_7O^+$). Finally, the product ion *m/z* 72 ($C_3H_6NO^+$) corresponds to a linear side-chain structure, as shown in Figure 7.

The fragmentation yield is sensitive to chirality, especially for CO loss or iminium formation, as previously observed for cyclo (Phe-Phe)H^+.[61] Loss of CO leading to the *m/z* 233 fragment is more efficient in the c-LDH^+ diastereomer at low collision energy. At higher collision energy, *m/z* 233 becomes more intense for c-LLH^+. This is probably due to larger fragmentation efficiency for c-LDH^+, which results in more abundant secondary fragments, hence less intense primary fragments. Iminium formation (*m/z* 136) and C_α-C_β cleavage of the tyrosine (*m/z* 155) are also more efficient in c-LDH^+. Pathways involving loss of NH_3 seem to be less sensitive to chirality and the *m/z* 244 or *m/z* 188 ion yield is similar for the two diastereomers.

The analysis of chemical dynamics trajectories allows the identification of intermediate states shown in Figure 8. Figure 8 display the reagent, denoted as REAG-01 and corresponding to the most stable c-LLH^+ or c-LDH^+, as well as the intermediate states that successively appear in the trajectories. We will first analyze these results qualitatively: the DKP ring opens up during the first isomerization step; all the intermediate states are therefore linear and bear a single chiral center. The intermediate states obtained starting from c-LLH^+ and c-LDH^+ are therefore expected to be enantiomers to each other and have the same energy. The reaction energy is therefore almost identical for c-LLH^+ and c-LDH^+, the only difference being the difference between the most stable isomer of c-LLH^+ and c-LDH^+. This would result in a slightly larger fragmentation of c-LDH^+, in line with the experimental observations. The difference is limited, precisely because after the first reaction step leading to the intermediate states shown in Figure 8, the two systems issued from c-LLH^+ and c-LDH^+ evolve on identical potential energy surfaces. As mentioned before, this is because the system bears a single chiral center from the first reaction step on. This explanation is only qualitative, as it does not take into account the barrier leading to this first intermediate, which is the step responsible for the stereoselectivity of the reaction. For more quantitative analysis, we have therefore optimized all the structures shown in Figure 8 and determined the structure and energy of the transition state between them. The corresponding values are given in Figure S2 in the Supplementary Information. These energy values must be taken with caution for the following reasons: first, due to computational cost, the calculations are performed at a lower level (6-31G(d,p)) than the optimization of the conformers of c-LLH^+ and c-LDH^+, which introduces some uncertainty on the calculated values. For example, the energy difference between c-LDH^+ and c-LLH^+ is 0.5 kcal/mol at the 6-311++G(d,p) level and 1.6 kcal/mol at the 6-31G(d,p) level. Second, the reaction path depicted in Figure 8 is one reaction path among others obtained from simulations, but, due to the complexity of the potential energy surface, it is possible that lower-energy pathways exist.

Then, using RRKM theory, we calculated the rate constants corresponding to the first steps: from reactant to first intermediate (k_{12}), the back reaction (k_{21}) and the reaction involving the step connecting the first intermediate with the following one (k_{23}), from which we assume the reaction is done and where the two surfaces are almost identical. RRKM rate constants rest on numerous hypotheses, among which the equilibrium of the reactants, which might be not fulfilled in our experimental conditions in particular concerning reactions starting from intermediate ions. A complete theoretical study of the reaction is beyond the scope of this paper. However, qualitative information can be drawn from the energetics shown in Figure S2 and the RRKM results shown in Figure 9. First, the rate-limiting steps are at the early stage of the reaction, which can be described in terms of concomitant C_4-N cleavage (opening of the peptide ring) and *cis* - *trans* isomerization of the peptide bond. The following steps involve less energetically demanding proton transfer or large-amplitude motions of the substituents. Second, the energy values associated with the first step (transition state and intermediate Int01) are different for c-LDH$^+$ and c-LLH$^+$. Then, the difference vanishes, as mentioned above, because the two systems evolve on enantiomeric potential energy surfaces. Last, analysis of the RRKM results shows that $k_{21} > k_{23}$ for c-LLH$^+$ while $k_{23} > k_{21}$ for c-LDH$^+$. In other words, the reaction tends to go forwards for c-LDH$^+$ while the back reaction towards the reactants is more efficient in c-LLH$^+$, which is compatible with the slightly larger fragmentation efficiency observed experimentally for c-LDH$^+$.

3. Vibrational Spectroscopy and Structure of the Dimer

The IRMPD spectra of the c-LL and c-LD protonated dimers are shown in Figure 10. The two diastereoisomers exhibit identical IRMPD features within the error. First, the fingerprint region is dominated by two intense bands in the region of the β(OH) and β(OH$^+$) bending modes, which look identical for the two dimers (1186/1184 and 1283/1281 cm^{-1}) and an intense band corresponding at the ν(CO) stretch region at ~1740 cm^{-1}. Between these bands, three bands of weaker intensity appear at a similar position as in the monomer. In the high-frequency region, the spectra are dominated by two intense and narrow bands corresponding to the NH stretch at ~3430 cm^{-1} and to the phenol OH stretch at ~3640 cm^{-1}.

The spectra of the dimers are very close to those of the monomers recorded at low laser intensity, except that the ν(OH$^+$) stretch bands observed for the monomer in the 3550 - 3600 cm^{-1} range disappear in the dimers. This suggests that the two monomers are linked by an

OH^+…X interaction. Moreover, the ν(NH) and ν(CO) stretch frequencies appear at the same position as in the monomer, which allows excluding the formation of dimers involving two intramolecular NH…OC bonds, as it is the case for the neutral cyclo (Phe-Phe) dimer.[97]

Because the experimental spectra of the protonated dimers are identical for c-LL and c-LD, we have performed calculations for c-LL only. Several starting structures of the dimer were considered, which can be classified into different families depending on the proton location. For each of these families, folded or extended geometries of the hydroxy-benzyl substituent were considered. The families with the proton on the proline nitrogen are, as mentioned for the monomer, much less stable than those with the proton located on either of the amide CO groups. The structures involving an NH^+…N interaction are above the global minimum by more than 25 kcal/mol. Those involving an OH^+…N or NH^+…O interaction are calculated between 16 and 20 kcal/mol above the global minimum. These structures will not be discussed further.

Numerous structures are found below 5 kcal/mol, with the proton located on the proline or tyrosine oxygen, and forming a strong hydrogen bond with either the proline or tyrosine oxygen of the second c-LL, which results in a shared proton (see Figure 11). Although protonation on the proline oxygen is less stable in the monomer, the structure with a shared proton between the two proline oxygen atoms, $OH^+_{Pro}…O_{Pro}$, is not very high in energy (2.1 kcal/mol,) and deserves to be discussed. Its stability stems from the folded position of the phenol substituents, which allows their OH groups to interact with each other. However, the interaction between the two hydroxyls should lead to two different ν(OH) frequencies, at odd with the experimental results. Therefore, we can discard this structure. The structures with shared proton between the tyrosine and proline oxygen atoms encompass the most stable structure, $OH^+_{Tyr}…O_{Pro}$. This structure is stabilized by the interaction between an aromatic OH and the other part of the dimer, which does not account for the experimental result.

All the other stable structures below 5 kcal/mol correspond to a shared proton between the two tyrosine amide oxygen atoms. In these structures, there is no strong energetic preference for neither folded nor extended orientation of the aromatic substituent. These structures will be called $OH^+_{Tyr}…O_{Tyr}$, with the index E when the aromatic substituent is extended. Each of these structures displays two variants, depending on the lone pair of the CO involved in the hydrogen bond. The structures with the two aromatic rings on opposite sides of the hydrogen bond will be denoted by " to differentiate them from those with the two aromatic rings on the same side of the hydrogen bond. The folded structures are more stable than the extended structures. More stability is also observed for the structures with the two aromatic substituents on the same side of the hydrogen bond. The best match with the experiment is obtained for the spectra of

$OH_{Tyr}…O_{TyrE}$ and $OH_{TyrE}…O_{Tyr}$", shown in Figure 10 together with the experiment. A disagreement in the intensity of the lower-energy band is observed. This can be due to saturation effects, as observed already for the monomer for which the intensity of these bands was underestimated in the calculations compared to the spectrum recorded at high laser intensity. These structures are the two variants with aromatic rings on the same or on opposite sides of the hydrogen bond of a dimer with a shared proton between the two tyrosine CO. One of the monomers is folded while the other one has the extended structure that is the most stable in the neutral monomer.

The cohesion of the proton-bound dimer results from a single strong hydrogen bond, which can be seen as a shared proton.[129-131] The description of this strong interaction is very challenging and requires theoretical developments that go beyond the harmonic approximation.[132] The vibrational modes are indeed very anharmonic, which explains the non-perfect match between the experiment and the calculations in the fingerprint region. On the other hand, the subunits contained in the dimer are not those that are chirality sensitive. Indeed, the $OH^+…\pi$ interaction responsible for the difference between c-LLH^+ and c-LDH^+ does not longer exist in the dimer due to the involvement of OH^+ in the intermolecular interaction. This, added to the presence of a single interaction between the two moieties, makes the spectrum of the protonated dimer identical for c-LL and c-LD.

Conclusion

The IRMPD spectrum of both protonated c-LLH^+ and c-LDH^+ monomers is well reproduced by several conformers that all have the proton localized on the amide oxygen of the tyrosine residue. The structures with the proton at other protonation sites, *i.e.*, oxygen of the proline or nitrogen, are much higher in energy and are not observed in our experimental conditions. The most stable structure is common to c-LLH^+ and c-LDH^+ and is an extended structure stabilized by an $OH^+…\pi$ intramolecular interaction, which is stronger in c-LLH^+. Additional conformers contribute to the experimental spectrum, with the benzyl ring folded over the DKP ring, and different orientation, *cis* or *trans*, of the proton. These conformers are stabilized by a weak CH…π interaction. Their relative energy is below 2 kcal/mol for c-LDH^+ and ~5 kcal/mol for c-LLH^+, which points towards a larger flexibility of c-LDH^+, as already supposed for other peptides. However, the gas-phase energies must be taken with caution and the observed spectrum probably reflect the structure in solution that is kinetically trapped.

In addition to the energetics, small structural differences are observed between c-LLH$^+$ and c-LDH$^+$. The folded conformers differ in the nature of the CH… π interaction, as do the neutral species, which has no consequence on the IR spectra.

cyclo (Tyr-Pro) contrasts with cyclo (Phe-Phe) in which neutral and protonated forms have similar most stable structures. In cyclo (Tyr-Pro), the most stable neutral structure is folded while the most stable protonated form is an extended structure. Moreover, neutral cyclo (Tyr-Pro) stands out among the DKP dipeptides we have studied as it shows heterochiral preference. The Gibbs energy of neutral c-LD is 2 kcal/mol lower than that of neutral c-LL. The opposite is true in the protonated form and the homochiral c-LLH$^+$ form is the most stable. The presence of the proton allows unfolding the molecule, which in turn results in larger stability of c-LLH$^+$ *vs.* c-LDH$^+$. Also, the extended structures show more distinct spectroscopic signatures for c-LLH$^+$ *vs.* c-LDH$^+$ than the folded structures in the neutral forms do, or the most stable structure in protonated cyclo (Phe-Phe) does. Interestingly, the extended structure is the most differentiating one in terms of chirality and the most stable one in protonated cyclo (Tyr-Pro). This contrasts with protonated cyclo (Phe-Phe) in which higher-energy structures were the discriminating ones. Whether the most stable forms or higher-energy structures are responsible for chiral discrimination has been discussed already for explaining chiral-phase chromatography separation mechanisms.[133]

While the c-LL and c-LD protonated monomers show distinct spectroscopic signatures, this is not the case for the protonated dimer. The lack of discrimination in the dimer arises from two points: first, there is a single strong OH$^+$…O interaction, which makes the system floppy and not specific as observed for the protonated complex between camphor and alanine or for amino acid dimers.[134, 135] Second, the sub-units contained in the dimer are precisely those that are not selective, *i.e.*, the folded protonated subunit and the extended neutral monomer.

The larger stability of c-LLH$^+$ is also manifested by a slightly larger fragmentation efficiency for c-LD H$^+$. This difference can be rationalized in terms of different reactant energies, c-LLH$^+$ being more stable, but identical intermediate states after the first reaction step. This intermediate step results from the opening of the DKP ring. As a result, it only bears one chiral center, which explains that its energy is the same for the c-LLH$^+$ and c-LDH$^+$ reagents. After this first reaction step, the two diastereomer systems evolve on identical potential energy surfaces, which in turn explains the limited sensitivity of the fragmentation process to stereochemical factors. This observation paves the way to further studies of stereochemical effects in DKP-based molecules, which are currently in progress.

Acknowledgements

We thank Dr. J. M. Ortega and the CLIO team for technical assistance. We thank F. Gobert for experimental help. We acknowledge the use of the computing facility cluster MésoLUM of the LUMAT federation (FR LUMAT 2764). AFPM and RS thank ANR DynBioReact (Grant No. ANR-14-CE06-0029-01) for financial support. The research described here has been supported by the Investissements d'Avenir LabEx PALM contract (ANR-10-LABX-0039-PALM).

References

[1] G.R. Desiraju, T. Steiner, The Weak Hydrogen Bond in Structural Chemistry and Biology, Oxford University Press, New York, USA, 1999.
[2] K. Schwing, M. Gerhards, Investigations on isolated peptides by combined IR/UV spectroscopy in a molecular beam - structure, aggregation, solvation and molecular recognition, International Reviews in Physical Chemistry, 35 (2016) 569-677.
[3] E. Gloaguen, M. Mons, Isolated Neutral Peptides, in: A.M. Rijs, J. Oomens (Eds.) Gas-Phase Ir Spectroscopy and Structure of Biological Molecules, 2015, pp. 225-270.
[4] T.S. Zwier, Laser probes of conformational isomerization in flexible molecules and complexes, Journal of Physical Chemistry A, 110 (2006) 4133-4150.
[5] A. Perez-Mellor, I. Alata, V. Lepere, A. Zehnacker, Conformational Study of the Jet-Cooled Diketopiperazine Peptide Cyclo Tyrosyl-Prolyl, Journal of Physical Chemistry B, 123 (2019) 6023-6033.
[6] M. Alauddin, E. Gloaguen, V. Brenner, B. Tardivel, M. Mons, A. Zehnacker-Rentien, V. Declerck, D.J. Aitken, Intrinsic Folding Proclivities in Cyclic -Peptide Building Blocks: Configuration and Heteroatom Effects Analyzed by Conformer-Selective Spectroscopy and Quantum Chemistry, Chemistry-a European Journal, 21 (2015) 16479-16493.
[7] K. Schwing, C. Reyheller, A. Schaly, S. Kubik, M. Gerhards, Structural Analysis of an Isolated Cyclic Tetrapeptide and its Monohydrate by Combined IR/UV Spectroscopy, ChemPhysChem, 12 (2011) 1981-1988.
[8] A. Perez-Mellor, I. Alata, V. Lepere, A. Zehnacker, Chirality effects in the structures of jet-cooled bichromophoric dipeptides, Journal of Molecular Spectroscopy, 349 (2018) 71-84.
[9] A.M. Rijs, J. Oomens, Gas-Phase IR Spectroscopy and Structure of Biological Molecules, in: Topics in Current Chemistry, Springer International Publishing, 2015.
[10] S. Bakels, M.P. Gaigeot, A.M. Rijs, Gas-Phase Infrared Spectroscopy of Neutral Peptides: Insights from the Far-IR and THz Domain, Chemical Reviews, 120 (2020) 3233-3260.
[11] J.K. Martens, I. Compagnon, E. Nicol, T.B. McMahon, C. Clavaguéra, G. Ohanessian, Globule to Helix Transition in Sodiated Polyalanines, Journal of Physical Chemistry Letters, 3 (2012) 3320-3324.
[12] J.A. Stearns, M. Guidi, O.V. Boyarkin, T.R. Rizzo, Conformation-specific infrared and ultraviolet spectroscopy of tyrosine-based protonated dipeptides, Journal of Chemical Physics, 127 (2007) 154322.
[13] S. Soorkia, C. Dehon, S.S. Kumar, M. Pedrazzani, E. Frantzen, B. Lucas, M. Barat, J.A. Fayeton, C. Jouvet, UV Photofragmentation Dynamics of Protonated Cystine: Disulfide Bond Rupture, Journal of Physical Chemistry Letters, 5 (2014) 1110-1116.

[14] L. Joly, R. Antoine, A.R. Allouche, M. Broyer, J. Lemoine, P. Dugourd, Ultraviolet spectroscopy of peptide and protein polyanions in vacuo: Signature of the ionization state of tyrosine, Journal of the American Chemical Society, 129 (2007) 8428-+.
[15] J.P. Reilly, Ultraviolet Photofragmentation of Biomolecular Ions, Mass Spectrometry Reviews, 28 (2009) 425-447.
[16] J.S. Brodbelt, Photodissociation mass spectrometry: new tools for characterization of biological molecules, Chemical Society Reviews, 43 (2014) 2757-2783.
[17] M.Z. Kamrath, E. Garand, P.A. Jordan, C.M. Leavitt, A.B. Wolk, M.J. Van Stipdonk, S.J. Miller, M.A. Johnson, Vibrational Characterization of Simple Peptides Using Cryogenic Infrared Photodissociation of H-2-Tagged, Mass-Selected Ions, Journal of the American Chemical Society, 133 (2011) 6440-6448.
[18] J.K. Eng, A.L. McCormack, J.R. Yates, AN APPROACH TO CORRELATE TANDEM MASS-SPECTRAL DATA OF PEPTIDES WITH AMINO-ACID-SEQUENCES IN A PROTEIN DATABASE, J. Am. Soc. Mass Spectrom., 5 (1994) 976-989.
[19] B. Paizs, S. Suhai, Fragmentation pathways of protonated peptides, Mass Spectrometry Reviews, 24 (2005) 508-548.
[20] V.H. Wysocki, G. Tsaprailis, L.L. Smith, L.A. Breci, Special feature: Commentary - Mobile and localized protons: a framework for understanding peptide dissociation, Journal of Mass Spectrometry, 35 (2000) 1399-1406.
[21] J.S. Brodbelt, Ion Activation Methods for Peptides and Proteins, Analytical Chemistry, 88 (2016) 30-51.
[22] R.A. Zubarev, Reactions of polypeptide ions with electrons in the gas phase, Mass Spectrometry Reviews, 22 (2003) 57-77.
[23] J.M. Wells, S.A. McLuckey, Collision-induced dissociation (CID) of peptides and proteins, in: A.L. Burlingame (Ed.) Biological Mass Spectrometry, 2005, pp. 148-185.
[24] A.K. Shukla, J.H. Futrell, Tandem mass spectrometry: dissociation of ions by collisional activation, Journal of Mass Spectrometry, 35 (2000) 1069-1090.
[25] T. Cao, M.K. Nguyen, S.V. Serafin, T.H. Morton, Stereochemical preferences in 4-center syn-eliminations from gaseous ions, Journal of Organic Chemistry, 73 (2008) 6099-6107.
[26] S.V. Serafin, R. Maranan, K.L. Zhang, T.H. Morton, Mass spectrometric differentiation of linear peptides composed of L-amino acids from isomers containing one D-amino acid residue, Analytical Chemistry, 77 (2005) 5480-5487.
[27] S.V. Serafin, K.L. Zhang, L. Aurelio, A.B. Hughes, T.H. Morton, Decomposition of protonated threonine, its stereoisomers, and its homologues in the gas phase: Evidence for internal backside displacement, Organic Letters, 6 (2004) 1561-1564.
[28] A. Marek, H.T.H. Nguyen, B. Broz, F. Turecek, Stereospecific control of peptide gas-phase ion chemistry with cis and trans cyclo ornithine residues, Journal of Mass Spectrometry, 53 (2018) 124-137.
[29] J.S. Splitter, F. Turecek, Applications of Mass Spectrometry to Organic Stereochemistry, in, VCH Publishers, New York, USA, 1994.
[30] A. Zehnacker, Chirality Effects in Gas-Phase Spectroscopy and Photophysics of Molecular and Ionic Complexes: Contribution of Low and Room Temperature Studies, International Reviews in Physical Chemistry, 33 (2014) 151-207.
[31] A. Bouchet, J. Klyne, S. Ishiuchi, M. Fujii, O. Dopfer, Conformation of protonated glutamic acid at room and cryogenic temperatures, Physical Chemistry Chemical Physics, 19 (2017) 10767-10776.
[32] A. Bouchet, J. Klyne, S.-i. Ishiuchi, O. Dopfer, M. Fujii, A. Zehnacker, Stereochemistry-dependent structure of hydrogen-bonded protonated dimers: the case of 1-amino-2-indanol, Physical Chemistry Chemical Physics, 20 (2018) 12430-12443.

[33] A. Bouchet, J. Klyne, G. Piani, O. Dopfer, A. Zehnacker, Diastereo-specific conformational properties of neutral, protonated and radical cation forms of (1R,2S)-cis- and (1R,2R)-trans-amino-indanol by gas phase spectroscopy, Physical Chemistry Chemical Physics, 17 (2015) 25809-25821.
[34] A. Filippi, A. Giardini, S. Piccirillo, M. Speranza, Gas-phase enantioselectivity, International Journal of Mass Spectrometry, 198 (2000) 137-163.
[35] M. Speranza, F. Gasparrini, B. Botta, C. Villani, D. Subissati, C. Fraschetti, F. Subrizi, Gas-phase enantioselective reactions in noncovalent ion-molecule complexes, Chirality, 21 (2009) 69-86.
[36] W.A. Tao, R.G. Cooks, Chiral analysis by MS, Analytical Chemistry, 75 (2003) 25A-31A.
[37] W.A. Tao, D.X. Zhang, E.N. Nikolaev, R.G. Cooks, Copper(II)-assisted enantiomeric analysis of D,L-amino acids using the kinetic method: Chiral recognition and quantification in the gas phase, Journal of the American Chemical Society, 122 (2000) 10598-10609.
[38] M. Tamura, T. Sekiguchi, S.-I. Ishiuchi, A. Zehnacker-Rentien, M. Fujii, Can the Partial Peptide SIVSF of beta2-Adrenergic Receptor Recognize Chirality of Epinephrine Neurotransmitter?, The journal of physical chemistry letters, (2019) 2470-2474.
[39] Y.J. Liang, J.S. Bradshaw, D.V. Dearden, The thermodynamic basis for enantiodiscrimination: Gas-phase measurement of the enthalpy and entropy of chiral amine recognition by dimethyldiketopyridino-18-crown-6, Journal of Physical Chemistry A, 106 (2002) 9665-9671.
[40] T. Sivaleela, M.R. Kumar, S. Prabhakar, G. Bhaskar, M. Vairamani, Chiral discrimination of alpha-amino acids by DNA tetranucleotides under electrospray ionization conditions, Rapid Communications in Mass Spectrometry, 22 (2008) 204-210.
[41] J.F. Gal, M. Stone, C.B. Lebrilla, Chiral recognition of non-natural alpha-amino acids, International Journal of Mass Spectrometry, 222 (2003) PII S1387-3806(1302)00992-00992.
[42] F.X. Sunahori, G. Yang, E.N. Kitova, J.S. Klassen, Y. Xu, Chirality recognition of the protonated serine dimer and octamer by infrared multiphoton dissociation spectroscopy, Physical Chemistry Chemical Physics, 15 (2013) 1873-1886.
[43] V. Scutelnic, M.A.S. Perez, M. Marianski, S. Warnke, A. Gregor, U. Rothlisberger, M.T. Bowers, C. Baldauf, G. von Helden, T.R. Rizzo, J. Seo, The Structure of the Protonated Serine Octamer, Journal of the American Chemical Society, 140 (2018) 7554-7560.
[44] J.L. Seymour, F. Turecek, A.V. Malkov, P. Kocovsky, Chiral recognition in solution and the gas phase. Experimental and theoretical studies of aromatic D- and L-amino acid-Cu(II)-chiragen complexes, Journal of Mass Spectrometry, 39 (2004) 1044-1052.
[45] A.G. Abo-Riziq, J.E. Bushnell, B. Crews, M.P. Callahan, L. Grace, M.S. de Vries, Discrimination between diastereoisomeric dipeptides by IR-UV double resonance spectroscopy and ab initio calculations, International Journal of Quantum Chemistry, 105 (2005) 437-445.
[46] E. Gloaguen, F. Pagliarulo, V. Brenner, W. Chin, F. Piuzzi, B. Tardivel, M. Mons, Intramolecular recognition in a jet-cooled short peptide chain: gamma-turn helicity probed by a neighbouring residue, Physical Chemistry Chemical Physics, 9 (2007) 4491-4497.
[47] E. Gloaguen, H. Valdes, F. Pagliarulo, R. Pollet, B. Tardivel, P. Hobza, F. Piuzzi, M. Mons, Experimental and Theoretical Investigation of the Aromatic-Aromatic Interaction in Isolated Capped Dipeptides, Journal of Physical Chemistry A, 114 (2010) 2973-2982.
[48] W.H. James, III, E.E. Baquero, V.A. Shubert, S.H. Choi, S.H. Gellman, T.S. Zwier, Single-Conformation and Diastereomer Specific Ultraviolet and Infrared Spectroscopy of Model Synthetic Foldamers: alpha/beta-Peptides, Journal of the American Chemical Society, 131 (2009) 6574-6590.
[49] W.H. James, E.E. Baquero, S.H. Choi, S.H. Gellman, T.S. Zwier, Laser Spectroscopy of Conformationally Constrained alpha/beta-Peptides: Ac-ACPC-Phe-NHMe and Ac-Phe-ACPC-NHMe, Journal of Physical Chemistry A, 114 (2010) 1581-1591.

[50] R. Sudha, M.F. Jarrold, Left-handed and ambidextrous helices in the gas phase, Journal of Physical Chemistry B, 109 (2005) 11777-11780.
[51] C.M. Adams, F. Kjeldsen, R.A. Zubarev, B.A. Budnik, K.F. Haselmann, Electron capture dissociation distinguishes a single D-amino acid in a protein and probes the tertiary structure, J. Am. Soc. Mass Spectrom., 15 (2004) 1087-1098.
[52] R.C. Dunbar, J.D. Steill, J. Oomens, Chirality-Induced Conformational Preferences in Peptide-Metal Ion Binding Revealed by IR Spectroscopy, Journal of the American Chemical Society, 133 (2011) 1212-1215.
[53] V. Lepere, K. Le Barbu-Debus, C. Clavaguéra, D. Scuderi, G. Piani, A.-L. Simon, F. Chirot, L. MacAleese, P. Dugourd, A. Zehnacker, Chirality-dependent structuration of protonated or sodiated polyphenylalanines: IRMPD and ion mobility studies, Physical Chemistry Chemical Physics, 18 (2016) 1807-1817.
[54] T. Vaisar, J. Urban, H. Nakanishi, Peptide diastereoisomers show different proton affinities, Journal of Mass Spectrometry, 31 (1996) 937-939.
[55] C. Afonso, J.C. Tabet, G. Giorgi, F. Turecek, Gas-phase doubly charged complexes of cyclic peptides with copper in+1,+2 and+3 formal oxidation states: formation, structures and electron capture dissociation, Journal of Mass Spectrometry, 47 (2012) 208-220.
[56] M. Lagarrigue, A. Bossee, C. Afonso, F. Fournier, B. Bellier, J.C. Tabet, Diastereomeric differentiation of peptides with CuII and FeII complexation in an ion trap mass spectrometer, Journal of Mass Spectrometry, 41 (2006) 1073-1085.
[57] P.J. Milne, A.L. Hunt, K. Rostoll, J.J. Van Der Walt, C.J.M. Graz, The biological activity of selected cyclic dipeptides, J. Pharm. Pharmacol., 50 (1998) 1331-1337.
[58] G. Kilian, H. Jamie, S.C.A. Brauns, K. Dyason, P.J. Milne, Biological activity of selected tyrosine-containing 2,5-diketopiperazines, Pharmazie, 60 (2005) 305-309.
[59] F. BenNasr, A. Perez-Mellor, I. Alata, V. Lepere, N.E. Jaidane, A. Zehnacker, Stereochemistry-dependent hydrogen bonds stabilise stacked conformations in jet-cooled cyclic dipeptides: (LD) vs. (LL) cyclo tyrosine-tyrosine, Faraday Discussions, 212 (2018) 399-419.
[60] S. Wiedemann, A. Metsala, D. Nolting, R. Weinkauf, The dipeptide cyclic(glycyltryptophanyl) in the gas phase: A concerted action of density functional calculations, S-0-S-1 two-photon ionization, spectral UV/UV hole burning and laser photoelectron spectroscopy, Physical Chemistry Chemical Physics, 6 (2004) 2641-2649.
[61] I. Alata, A. Perez-Mellor, F. Ben Nasr, D. Scuderi, V. Steinmetz, F. Gobert, N.E. Jaidane, A. Zehnacker-Rentien, Does the Residues Chirality Modify the Conformation of a Cyclo-Dipeptide? Vibrational Spectroscopy of Protonated Cyclo-diphenylalanine in the Gas Phase, Journal of Physical Chemistry A, 121 (2017) 7130-7138.
[62] K.L. Carlson, S.L. Lowe, M.R. Hoffmann, K.A. Thomasson, Theoretical UV circular dichroism of aliphatic cyclic dipeptides, Journal of Physical Chemistry A, 109 (2005) 5463-5470.
[63] A.G. Abo-Riziq, B. Crews, J.E. Bushnell, M.P. Callahan, M.S. De Vries, Conformational analysis of cyclo(Phe-Ser) by UV-UV and IR-UV double resonance spectroscopy and ab initio calculations, Molecular Physics, 103 (2005) 1491-1495.
[64] D. Wang, K. Gulyuz, C.N. Stedwell, N.C. Polfer, Diagnostic NH and OH Vibrations for Oxazolone and Diketopiperazine Structures: b(2) from Protonated Triglycine, J. Am. Soc. Mass Spectrom., 22 (2011) 1197-1203.
[65] S. Zou, J. Oomens, N.C. Polfer, Competition between diketopiperazine and oxazolone formation in water loss products from protonated ArgGly and GlyArg, International Journal of Mass Spectrometry, 316 (2012) 12-17.
[66] J.C. Poutsma, J. Martens, J. Oomens, P. Maitre, V. Steinmetz, M. Bernier, M.X. Jia, V. Wysocki, Infrared Multiple-Photon Dissociation Action Spectroscopy of the b(2)(+) Ion from

PPG: Evidence of Third Residue Affecting b(2)(+) Fragment Structure, J. Am. Soc. Mass Spectrom., 28 (2017) 1482-1488.
[67] M.C. Bernier, J. Chamot-Rooke, V.H. Wysocki, R vs. S fluoroproline ring substitution: trans/cis effects on the formation of b(2) ions in gas-phase peptide fragmentation, Physical Chemistry Chemical Physics, 18 (2016) 2202-2209.
[68] S.H. Yoon, J. Chamot-Rooke, B.R. Perkins, A.E. Hilderbrand, J.C. Poutsma, V.H. Wysocki, IRMPD Spectroscopy Shows That AGG Forms an Oxazolone b(2)(+) Ion, Journal of the American Chemical Society, 130 (2008) 17644-+.
[69] J. Oomens, S. Young, S. Molesworth, M. van Stipdonk, Spectroscopic Evidence for an Oxazolone Structure of the b(2) Fragment Ion from Protonated Tri-Alanine, J. Am. Soc. Mass Spectrom., 20 (2009) 334-339.
[70] N.C. Polfer, J. Oomens, S. Suhai, B. Paizs, Spectroscopic and theoretical evidence for oxazolone ring formation in collision-induced dissociation of peptides, Journal of the American Chemical Society, 127 (2005) 17154-17155.
[71] P.Y.I. Shek, J.K.-C. Lau, J. Zhao, J. Grzetic, U.H. Verkerk, J. Oomens, A.C. Hopkinson, K.W.M. Siu, Fragmentations of protonated cyclic-glycylglycine and cyclic-alanylalanine, International Journal of Mass Spectrometry, 316 (2012) 199-205.
[72] A. Pérez Mellor, R. Spezia, Determination of kinetic properties in unimolecular dissociation of complex systems from graph-theory based analysis of an ensemble of reactive trajectories., Manuscrpt in preparation.
[73] E. Gross, The Peptides Analysis, Synthesis, Biology: Modern Techniques of Conformational Structural, and Configurational Analysis, in: Elsevier, 2012.
[74] A. Pérez Mellor, A. Zehnacker, Chirality Effects in Jet-Cooled Cyclic Dipeptides, in: T. Ebata, M. Fujii (Eds.) Physical Chemistry of Cold Gas-Phase Functional Molecules and Clusters, Springer, Singapore, 2019, pp. 63-87.
[75] S.G. Stepanian, I.D. Reva, E.D. Radchenko, L. Adamowicz, Conformers of nonionized proline. Matrix-isolation infrared and post-Hartree-Fock ab initio study, Journal of Physical Chemistry A, 105 (2001) 10664-10672.
[76] R.H. Wu, T.B. McMahon, Infrared multiple photon dissociation spectra of proline and glycine proton-bound homodimers. Evidence for zwitterionic structure, Journal of the American Chemical Society, 129 (2007) 4864-+.
[77] R.H. Wu, T.B. McMahon, An Investigation of Protonation Sites and Conformations of Protonated Amino Acids by IRMPD Spectroscopy, ChemPhysChem, 9 (2008) 2826-2835.
[78] M.E. Crestoni, B. Chiavarino, D. Scuderi, A. Di Marzio, S. Fornarini, Discrimination of 4-Hydroxyproline Diastereomers by Vibrational Spectroscopy of the Gaseous Protonated Species, Journal of Physical Chemistry B, 116 (2012) 8771-8779.
[79] S.J. Martinez, J.C. Alfano, D.H. Levy, The Electronic Spectroscopy of the Amino-Acids Tyrosine and Phenylalanine in a Supersonic Jet, Journal of Molecular Spectroscopy, 156 (1992) 421-430.
[80] R. Cohen, B. Brauer, E. Nir, L. Grace, M.S. de Vries, Resonance-enhanced multiphoton ionization spectroscopy of dipeptides, Journal of Physical Chemistry A, 104 (2000) 6351-6355.
[81] A. Abo-Riziq, L. Grace, B. Crews, M.P. Callahan, T. van Mourik, M.S. de Vries, Conformational Structure of Tyrosine, Tyrosyl-glycine, and Tyrosyl-glycyl-glycine by Double Resonance Spectroscopy, Journal of Physical Chemistry A, 115 (2011) 6077-6087.
[82] Y. Inokuchi, Y. Kobayashi, T. Ito, T. Ebata, Conformation of L-tyrosine studied by fluorescence-detected UV-UV and IR-UV double-resonance spectroscopy, Journal of Physical Chemistry A, 111 (2007) 3209-3215.
[83] Y. Shimozono, K. Yamada, S. Ishiuchi, K. Tsukiyama, M. Fujii, Revised conformational assignments and conformational evolution of tyrosine by laser desorption supersonic jet laser spectroscopy, Physical Chemistry Chemical Physics, 15 (2013) 5163-5175.

[84] C.M. Choi, D.H. Choi, N.J. Kim, J. Heo, Effective temperature of protonated tyrosine ions in a cold quadrupole ion trap, International Journal of Mass Spectrometry, 314 (2012) 18-21.
[85] S. Soorkia, M. Broquier, G. Gregoire, Conformer- and Mode-Specific Excited State Lifetimes of Cold Protonated Tyrosine Ions, Journal of Physical Chemistry Letters, 5 (2014) 4349-4355.
[86] S. Ishiuchi, H. Wako, D. Kato, M. Fujii, High-cooling-efficiency cryogenic quadrupole ion trap and UV-UV hole burning spectroscopy of protonated tyrosine, Journal of Molecular Spectroscopy, 332 (2017) 45-51.
[87] P.J. Milne, D.W. Oliver, H.M. Roos, Cyclodipeptides - Structure and Conformation of Cyclo(Tyrosyl Prolyl), J Cryst Spectrosc, 22 (1992) 643-649.
[88] P.E. Young, V. Madison, E.R. Blout, Cyclic peptides. 15. Lanthanide-assisted carbon-13 and proton NMR analysis of preferred side-chain rotamers in proline-containing cyclic dipeptides, Journal of the American Chemical Society, 98 (1976) 5365-5371.
[89] J.M. Bakker, T. Besson, J. Lemaire, D. Scuderi, P. Maitre, Gas-phase structure of a pi-allyl-palladium complex: Efficient infrared Spectroscopy in a 7 T Fourier transform mass spectrometer, Journal of Physical Chemistry A, 111 (2007) 13415-13424.
[90] R. Prazeres, F. Glotin, C. Insa, D.A. Jaroszynski, J.M. Ortega, Two-colour operation of a Free-Electron Laser and applications in the mid-infrared, European Physical Journal D, 3 (1998) 87-93.
[91] L. Goerigk, S. Grimme, A thorough benchmark of density functional methods for general main group thermochemistry, kinetics, and noncovalent interactions, Physical Chemistry Chemical Physics, 13 (2011) 6670-6688.
[92] M.J. Frisch, J.A. Pople, J.S. Binkley, Self-Consistent Molecular-Orbital Methods .25. Supplementary Functions for Gaussian-Basis Sets., Journal of Chemical Physics, 80 (1984) 3265-3269.
[93] M.D. Halls, J. Velkovski, H.B. Schlegel, Harmonic frequency scaling factors for Hartree-Fock, S-VWN, B-LYP, B3-LYP, B3-PW91 and MP2 with the Sadlej pVTZ electric property basis set., Theoretical Chemistry Accounts, 105 (2001) 413.
[94] N. Mohan, K.P. Vijayalakshmi, N. Koga, C.H. Suresh, Comparison of Aromatic NH ...π, OH ...π, and CH ...π Interactions of Alanine Using MP2, CCSD, and DFT Methods, Journal of Computational Chemistry, 31 (2010) 2874-2882.
[95] J. Altnoeder, A. Bouchet, J.J. Lee, K.E. Otto, M.A. Suhm, A. Zehnacker-Rentien, Chirality-dependent balance between hydrogen bonding and London dispersion in isolated (+-)-1-indanol clusters, Physical Chemistry Chemical Physics, 15 (2013) 10167-10180.
[96] M. Walker, A.J.A. Harvey, A. Sen, C.E.H. Dessent, Performance of M06, M06-2X, and M06-HF Density Functionals for Conformationally Flexible Anionic Clusters: M06 Functionals Perform Better than B3LYP for a Model System with Dispersion and Ionic Hydrogen-Bonding Interactions, Journal of Physical Chemistry A, 117 (2013) 12590-12600.
[97] A. Perez-Mellor, A. Zehnacker, Vibrational circular dichroism of a 2,5-diketopiperazine (DKP) peptide: Evidence for dimer formation in cyclo LL or LD diphenylalanine in the solid state, Chirality, 29 (2017) 89-96.
[98] R.J. Plowright, E. Gloaguen, M. Mons, Compact Folding of Isolated Four-Residue Neutral Peptide Chains: H-Bonding Patterns and Entropy Effects, ChemPhysChem, 12 (2011) 1889-1899.
[99] M.J. Frisch, G.W. Trucks, H.B. Schlegel, G.E. Scuseria, M.A. Robb, J.R. Cheeseman, G. Scalmani, V. Barone, B. Mennucci, G.A. Petersson, H. Nakatsuji, M. Caricato, X.J. Li, H.P. Hratchian, A.F. Izmaylov, J. Bloino, G. Zheng, J.L. Sonnenberg, M. Hada, M. Ehara, K. Toyota, R. Fukuda, J. Hasegawa, M. Ishida, T. Nakajima, Y. Honda, O. Kitao, H. Nakai, T. Vreven, J. Montgomery, J. A. , J.E. Peralta, F. Ogliaro, M. Bearpark, J.J. Heyd, E. Brothers, K.N. Kudin, V.N. Staroverov, R. Kobayashi, J. Normand, K. Raghavachari, A. Rendell, J.C.

Burant, S.S. Iyengar, J. Tomasi, M. Cossi, N. Rega, J.M. Millam, M. Klene, J.E. Knox, J.B. Cross, V. Bakken, C. Adamo, J. Jaramillo, R. Gomperts, R.E. Stratmann, O. Yazyev, A.J. Austin, R. Cammi, C. Pomelli, J.W. Ochterski, R.L. Martin, K. Morokuma, V.G. Zakrzewski, G.A. Voth, P. Salvador, J.J. Dannenberg, S. Dapprich, A.D. Daniels, O. Farkas, J.B. Foresman, J.V. Ortiz, J. Cioslowski, D.J.S. Fox, Gaussian 09, Revision D.01, in, Gaussian Inc., Wallingford CT, 2009, pp. Gaussian 09, Revision A.02.
[100] S.O. Meroueh, Y.F. Wang, W.L. Hase, Direct dynamics Simulations of collision- and surface-induced dissociation of N-protonated glycine. Shattering fragmentation, Journal of Physical Chemistry A, 106 (2002) 9983-9992.
[101] A.M. Somer, V. Macaluso, G.L. Barnes, L. Yang, S. Pratihar, K. Song, W.L. Hase, R. Spezia, Role of Chemical Dynamics Simulations in Mass Spectrometry Studies of Collision-Induced Dissociation and Collisions of Biological Ions with Organic Surfaces, J. Am. Soc. Mass Spectrom., 31 (2020) 2-24.
[102] W.L. Hase, D.G. Buckowski, Monte-Carlo Sampling of A Micro-Canonical Ensemble of Classical Harmonic-Oscillators., Chemical Physics Letters, 74 (1980) 284-287.
[103] S. Grimme, Accurate description of van der Waals complexes by density functional theory including empirical corrections, Journal of Computational Chemistry, 25 (2004) 1463-1473.
[104] G.B. Rocha, R.O. Freire, A.M. Simas, J.J.P. Stewart, RM1: A reparameterization of AM1 for H, C, N, O, P, S, F, Cl, Br, and I, Journal of Computational Chemistry, 27 (2006) 1101-1111.
[105] L. Verlet, Computer Experiments on Classical Fluids .I. Thermodynamical Properties of Lennard-Jones Molecules., Physical Review, 159 (1967) 98-+.
[106] W.L. Hase, R.J. Duchovic, X. Hu, A. Komornicki, K.F. Lim, D.-H. Lu, G.H. Peslherbe, K.N. Swamy, S.R. Vande Linde, L. Zhu, A. Varandas, H. Wang, R. Wolf, VENUS96: A general chemical dynamics computer program. , QCPE Bull., 16 (1996) 43.
[107] J.J.P. Stewart, L.J. Fiedler, P. Zhang, J. Zheng, I. Rossi, W.-P. Hu, G.C. Lynch, Y.-P. Liu, Y.Y. Chuang, J. Pu, J. Li, C.J. Cramer, P.L. Fast, D.G. Truhlar, MOPAC 5.022mn., in, Department of Chemistry and Supercomputing Institute, University of Minnesota, Minneapolis, Department of Chemistry and Supercomputing Institute, University of Minnesota, Minneapolis, 2015.
[108] R. Spezia, A. Martin-Somer, V. Macaluso, Z. Homayoon, S. Pratihar, W.L. Hase, Unimolecular dissociation of peptides: statistical vs. non-statistical fragmentation mechanisms and time scales, Faraday Discussions, 195 (2016) 599-618.
[109] Y. Jeanvoine, A. Largo, W.L. Hase, R. Spezia, Gas Phase Synthesis of Protonated Glycine by Chemical Dynamics Simulations, Journal of Physical Chemistry A, 122 (2018) 869-877.
[110] B.D. McKay, A. Piperno, Practical graph isomorphism, II, Journal of Symbolic Computation, 60 (2014) 94-112.
[111] T. Baer, W.L. Hase, Unimolecular Reaction Dynamics: Theory and Experiments. , Oxford University Press, New York, 1996.
[112] T. Beyer, D.F. Swinehart, NUMBER OF MULTIPLY-RESTRICTED PARTITIONS, Communications of the Acm, 16 (1973) 379-379.
[113] W.L. Hase, L. Zhu, A general RRKM program., QCPE Bulletin, 14 (1994) 664.
[114] R.K. Sinha, B. Chiavarino, M.E. Crestoni, D. Scuderi, S. Fornarini, Tyrosine nitration as evidenced by IRMPD spectroscopy, International Journal of Mass Spectrometry, 308 (2011) 209-216.
[115] K. Hirata, Y. Mori, S.-I. Ishiuchi, M. Fujii, A. Zehnacker, Chiral discrimination between tyrosine and beta-cyclodextrin revealed by cryogenic ion trap infrared spectroscopy, Physical chemistry chemical physics : PCCP, 22 (2020) 24887-24894.

[116] O.V. Boyarkin, S.R. Mercier, A. Kamariotis, T.R. Rizzo, Electronic spectroscopy of cold, protonated tryptophan and tyrosine, Journal of the American Chemical Society, 128 (2006) 2816-2817.
[117] D. Scuderi, K. Le Barbu-Debus, A. Zehnacker, The role of weak hydrogen bonds in chiral recognition, Physical Chemistry Chemical Physics, 13 (2011) 17916-17929.
[118] A.E. Reed, L.A. Curtiss, F. Weinhold, Intermolecular interactions for a natural bond orbital, donor-acceptor viewpoint, Chemical Reviews, 88 (1988) 899-926.
[119] C.M. Leavitt, A.B. Wolk, J.A. Fournier, M.Z. Kamrath, E. Garand, M.J. Van Stipdonk, M.A. Johnson, Isomer-Specific IR-IR Double. Resonance Spectroscopy of D-2-Tagged Protonated Dipeptides Prepared in a Cryogenic Ion Trap, Journal of Physical Chemistry Letters, 3 (2012) 1099-1105.
[120] S.S. Lee, J.U. Lee, J.H. Oh, S. Park, Y. Hong, B.K. Min, H.H.L. Lee, H.I. Kim, X.L. Kong, S. Lee, H.B. Oh, Chiral differentiation of d- and l-isoleucine using permethylated -cyclodextrin: infrared multiple photon dissociation spectroscopy, ion-mobility mass spectrometry, and DFT calculations, Physical Chemistry Chemical Physics, 20 (2018) 30428-30436.
[121] L. Voronina, T.R. Rizzo, Spectroscopic studies of kinetically trapped conformations in the gas phase: the case of triply protonated bradykinin, Physical Chemistry Chemical Physics, 17 (2015) 25828-25836.
[122] E. Bodo, A. Ciavardini, A. Giardini, A. Paladini, S. Piccirillo, F. Rondino, D. Scuderi, Infrared multiple photon dissociation spectroscopy of ciprofloxacin: Investigation of the protonation site, Chemical Physics, 398 (2012) 124-128.
[123] M.J. van Stipdonk, M.J. Kullman, G. Berden, J. Oomens, Infrared multiple-photon dissociation spectroscopy of deprotonated 6-hydroxynicotinic acid, Rapid Communications in Mass Spectrometry, 28 (2014) 691-698.
[124] J. Tomasi, B. Mennucci, R. Cammi, Quantum mechanical continuum solvation models, Chemical Reviews, 105 (2005) 2999-3093.
[125] M. Lammerhofer, Chiral recognition by enantioselective liquid chromatography: Mechanisms and modern chiral stationary phases, Journal of Chromatography A, 1217 (2010) 814-856.
[126] S.M. Bratakos, V.J. Sinanoglou, M.T. Matsoukas, E. Siapi, D.P. Papahatjis, K. Riganakos, P. Zoumpoulakis, Fragmentation Patterns of Aromatic 2,5-diketopiperazines Using Liquid chromatography/Mass Spectrometry, Current Analytical Chemistry, 12 (2016) 439-449.
[127] Y.H. Chen, S.E. Liou, C.C. Chen, Two-step mass spectrometric approach for the identification of diketopiperazines in chicken essence, European Food Research and Technology, 218 (2004) 589-597.
[128] J. Vandergreef, A.C. Tas, L.M. Nijssen, J. Jetten, M. Hohn, Identification and Quantitation of Diketopiperazines by Liquid-Chromatography Mass-Spectrometry, Using a Moving Belt Interface, Journal of Chromatography, 394 (1987) 77-88.
[129] D.A. Thomas, M. Marianski, E. Mucha, G. Meijer, M.A. Johnson, G. von Helden, Ground-State Structure of the Proton-Bound Formate Dimer by Cold-Ion Infrared Action Spectroscopy, Angewandte Chemie-International Edition, 57 (2018) 10615-10619.
[130] T.D. Fridgen, L. MacAleese, P. Maitre, T.B. McMahon, P. Boissel, J. Lemaire, Infrared spectra of homogeneous and heterogeneous proton-bound dimers in the gas phase, Physical Chemistry Chemical Physics, 7 (2005) 2747-2755.
[131] D.T. Moore, J. Oomens, L. van der Meer, G. von Helden, G. Meijer, J. Valle, A.G. Marshall, J.R. Eyler, Probing the vibrations of shared, OH+O-bound protons in the gas phase, ChemPhysChem, 5 (2004) 740-743.
[132] C.H. Duong, N. Yang, P.J. Kelleher, M.A. Johnson, R.J. DiRisio, A.B. McCoy, Q. Yu, J.M. Bowman, B.V. Henderson, K.D. Jordan, Tag-Free and Isotopomer-Selective Vibrational

Spectroscopy of the Cryogenically Cooled H9O4+ Cation with Two-Color, IR-IR Double-Resonance Photoexcitation: Isolating the Spectral Signature of a Single OH Group in the Hydronium Ion Core, Journal of Physical Chemistry A, 122 (2018) 9275-9284.
[133] W.H. Pirkle, T.C. Pochapsky, Considerations of Chiral Recognition Relevant to the Liquid-Chromatographic Separation of Enantiomers., Chemical Reviews, 89 (1989) 347-362.
[134] A. Sen, K. Le Barbu-Debus, D. Scuderi, A. Zehnacker-Rentien, Mass Spectrometry Study and Infrared Spectroscopy of the Complex Between Camphor and the Two Enantiomers of Protonated Alanine: The Role of Higher-Energy Conformers in the Enantioselectivity of the Dissociation Rate Constants, Chirality, 25 (2013) 436-443.
[135] A. Andersson, M. Poline, M. Kodambattil, O. Rebrov, E. Loire, P. Maitre, V. Zhaunerchyk, Structure of Proton-Bound Methionine and Tryptophan Dimers in the Gas Phase Investigated with IRMPD Spectroscopy and Quantum Chemical Calculations, Journal of Physical Chemistry A, 124 (2020) 2408-2415.

		Name		ΔG (kcal/mol)	Name		ΔG (kcal/mol)
O-Protonated	Proline side	c-$g_{II}^{+}g^{-}$	(O_P^{+C})	9.5	c-$g_{II}^{+}g_D^{-}$	(O_P^{+C})	6.8
			(O_P^{+T})	7.0		(O_P^{+T})	4.2
		c-$g_{II}^{-}g^{-}$	(O_P^{+C})	8.9	c-$g_{II}^{-}g_D^{-}$	(O_P^{+C})	7.7
			(O_P^{+T})	7.5		(O_P^{+T})	6.4
		c-$t_{II}g^{-}$	(O_P^{+C})	13.6	c-$t_{II}g_D^{-}$	(O_P^{+C})	12.7
			(O_P^{+T})	11.5		(O_P^{+T})	10.5
	Tyrosine side	c-$g_{II}^{+}g^{-}$	(O_Y^{+C})	4.7	c-$g_{II}^{+}g_D^{-}$	(O_Y^{+C})	1.6
			(O_Y^{+T})	3.8		(O_Y^{+T})	0.5
		c-$g_{II}^{-}g^{-}$	(O_Y^{+C})	7.4	c-$g_{II}^{-}g_D^{-}$	(O_Y^{+C})	4.6
			(O_Y^{+T})	5.4		(O_Y^{+T})	3.3
		c-$t_{II}g^{-}$	(O_Y^{+C})	9.0	c-$t_{II}g_D^{-}$	(O_Y^{+C})	5.4
			(O_Y^{+T})	0.0		(O_Y^{+T})	0.1
		c-$g_{II}^{+}g^{-}$	(N_Y^{+})	16.3	c-$g_{II}^{-}g_D^{-}$	(N_Y^{+})	16.6
		c-$g_{II}^{+}g^{-}$	(N_P^{+T})	13.1	c-$g_{II}^{+}g_D^{-}$	(N_P^{+T})	11.7

Table 1: Relative Gibbs free energy ΔG of the most stable calculated structures for each protonation site, for type II hydroxyl orientation. The zero of the scale is taken at the most stable conformer for each diastereomer. The most stable c-LDH^+ conformer is 0.5 kcal/mol higher in energy than the most stable c-LLH^+. ΔG was calculated at standard ambient pressure and temperature: 298.15 K, 1 atm. Please note that the most stable isomer of c-LDH^+ belongs to the type I hydroxyl orientation and is not shown here.

Name	Rotamers	DKP ring						Proline ring					Interaction distance	
	τ	ϕ_1	ψ_1	ω_1	ϕ_2	ψ_2	ω_2	A	B	C	D	E		
c-$t_{II}g^-(O_Y{}^{+T})$	-178	-32	27	6	-34	29	2	3	-26	39	-36	21	2.51	$COH^+ \ldots \pi_Y$
c-$g_{II}{}^+g^-(O_Y{}^{+T})$	65	-7	17	-30	28	-16	7	-11	-15	35	-41	33	2.69	$C_{14}{}^{\beta}H \ldots \pi_Y$
c-$g_{II}{}^+g^-(O_Y{}^{+C})$	67	-9	17	-29	27	-15	8	-8	-18	36	-41	31	2.74	$C_{14}{}^{\beta}H \ldots \pi_Y$
c-$t_{II}g_D{}^-(O_Y{}^{+T})$	-179	26	-23	-2	24	-22	-3	0	24	-38	37	-24	2.60	$COH^+ \ldots \pi_Y$
c-$g_{II}{}^+g_D{}^-(O_Y{}^{+T})$	61	26	-19	-12	35	-28	-1	1	23	-39	38	-25	2.49	$C_3{}^{\alpha}H \ldots \pi_Y$
c-$g_{II}{}^+g_D{}^-(O_Y{}^{+C})$	62	27	-20	-12	35	-28	-1	1	24	-39	38	-25	2.47	$C_3{}^{\alpha}H \ldots \pi_Y$

Nomenclature

τ ($N\ C_1\ C_5\ C_6$) **ϕ_1** ($C_2\ N\ C_3\ C_4$) **ψ_1** ($N\ C_3\ C_4\ N$) **ω_1** ($C_3\ C_4\ N\ C_1$) **ϕ_2** ($C_4\ N\ C_1\ C_2$) **ψ_2** ($N\ C_1\ C_2\ N$) **ω_2** ($C_1\ C_2\ N\ C_3$)

A($C_3\ N\ C_{12}\ C_{13}$) **B**($N\ C_{12}\ C_{13}\ C_{14}$) **C**($C_{12}\ C_{13}\ C_{14}\ C_3$) **D**($C_{13}\ C_{14}\ C_3\ N$) **E**($C_{14}\ C_3\ N\ C_{12}$)

Table 2: Geometric parameters of the most stable structures. Angles are in degree (°) and distances in Angstroms (Å).

Experimental *m/z*	Molecular formula of the ionic fragment	Molecular formula of the neutral fragment	ΔE (kcal/mol)
261.12	$C_{14}H_{17}N_2O_3^+$		
244.10	$C_{14}H_{14}NO_3^+$	NH_3	15.4
233.13	$C_{13}H_{17}N_2O_2^+$	CO	63.3 (81.7)
216.10	$C_{13}H_{14}NO_2^+$	CH_3NO	56.5
		CO NH_3	29.9
205.13	$C_{12}H_{17}N_2O^+$	CO CO	(35.4)
188.11	$C_{12}H_{14}NO^+$	CH_3NO CO	69.6
		CO CO NH_3	43.0
186.09	$C_{12}H_{12}NO^+$	CH_3NO CO H_2	96.6
		CO CO NH_3 H_2	69.9
164.07	$C_9H_{10}NO_2^+$	C_5H_7NO	62.8
		C_4H_7N CO	72.8
155.08	$C_7H_{11}N_2O_2^+$	C_7H_6O	62.6
154.07	$C_7H_{10}N_2O_2^+$ [2]	C_7H_7O [2]	65.1
153.07	$C_7H_9N_2O_2^+$	C_7H_8O	81.6
147.04	$C_9H_7O_2^+$	$C_5H_{10}N_2O$	42.6
		C_4H_7N CH_3NO	96.6
		C_4H_7N CO NH_3	69.9
136.08	$C_8H_{10}NO^+$	$C_6H_7NO_2$	97.6
		C_5H_7NO CO	53.2
		C_4H_7N CO CO	63.3
119.05	$C_8H_7O^+$	C_4H_7N CH_3NO CO	126.9
107.05	$C_7H_7O^+$	$C_7H_{10}N_2O_2$	67.2
		$C_5H_6N_2O_2$ C_2H_4	116.7
		$C_4H_4N_2O_2$ C_3H_6	77.7
		$C_3H_3NO_2$ C_4H_7N	141.5
72.04	$C_3H_6NO^+$	$C_{11}H_{11}NO_2$	82.5

Table 3: Assignment of the *m/z* peaks experimentally observed to the ionic fragment resulting from the chemical dynamics simulations. The most abundant isomers of the product corresponding to each *m/z* peak is shown in Figure 7 for the ionic fragments and in Figure S1 of the supporting information for the neutral loss. For each *m/z* value, ΔE is the reaction energy computed at the DFT/B3LYP/6-311++g(d,p) level of the most stable isomer obtained by the chemical dynamic simulations. The values are relative to the most stable reagent c-t_{II}g- (O_Y^{+T}). The number in bracket is the spin multiplicity. When not specified otherwise, the value is one. The value in parenthesis is the formation energy of the ion-molecule complexes.

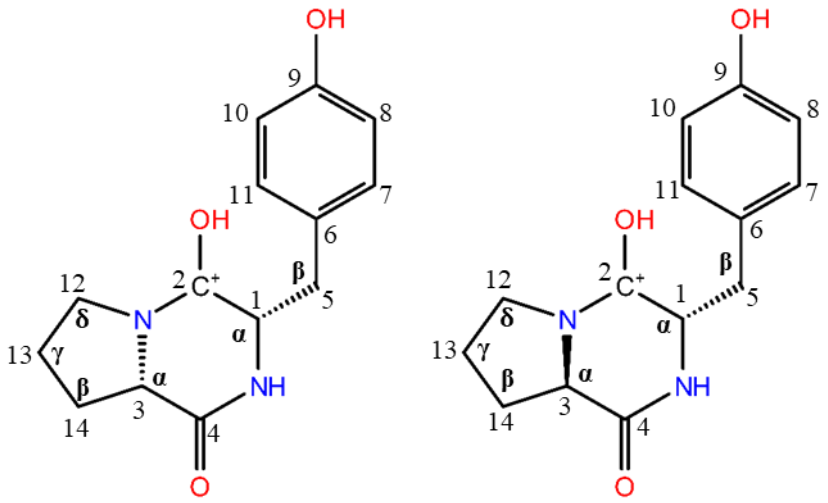

Figure 1. Structure of protonated cyclo (Tyr-Pro) and atom numbering, on the example of protonation at the amide oxygen of tyrosine.

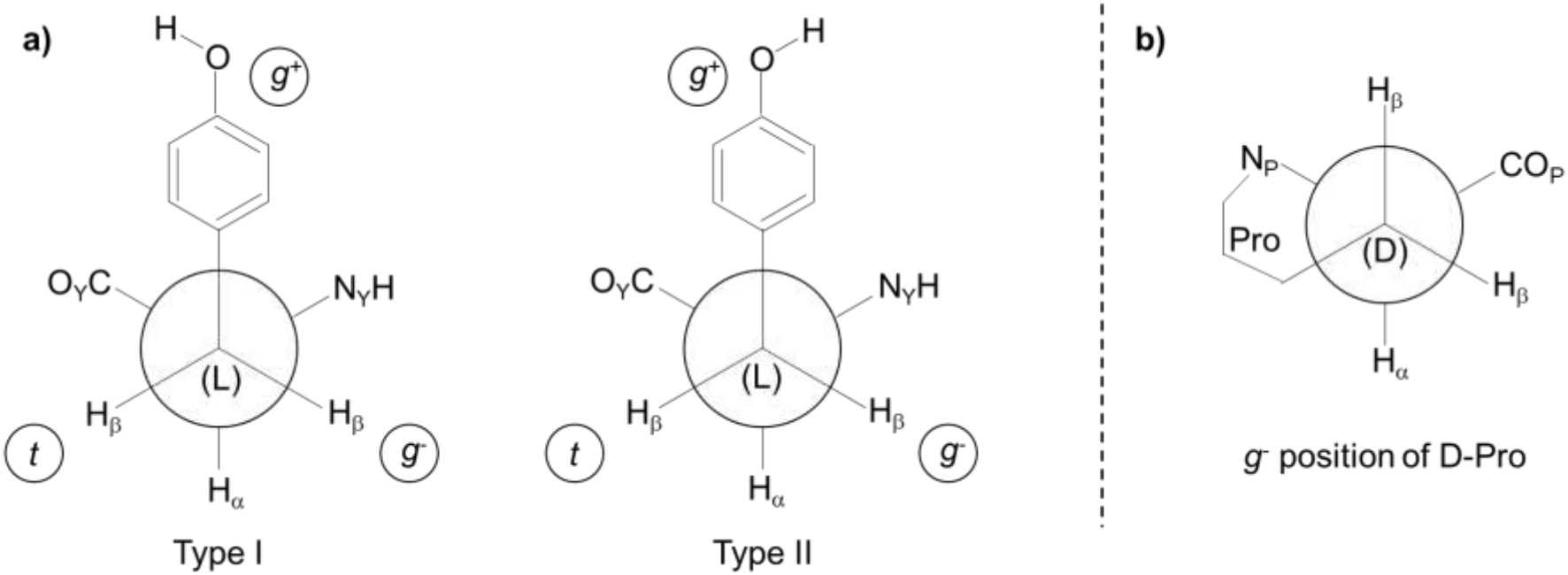

Figure 2. a) Newman projection along $C_{\alpha 1}C_{\beta 5}$ for L-tyrosine, with the hydroxy-benzyl in g^+ orientation. The possible orientations are indicated by circled letters g^-, g^+, and t. The hydroxyl geometry is denoted as type I for anticlockwise orientation or type II for clockwise orientation.
b) Newman projection along $C_{\alpha 3}C_{\beta 14}$ for D-proline showing the g^- conformation.
The different protonated sites are indicated by O_Y or O_P for oxygen protonation at the tyrosine or proline, respectively and N_Y or N_P for nitrogen protonation.

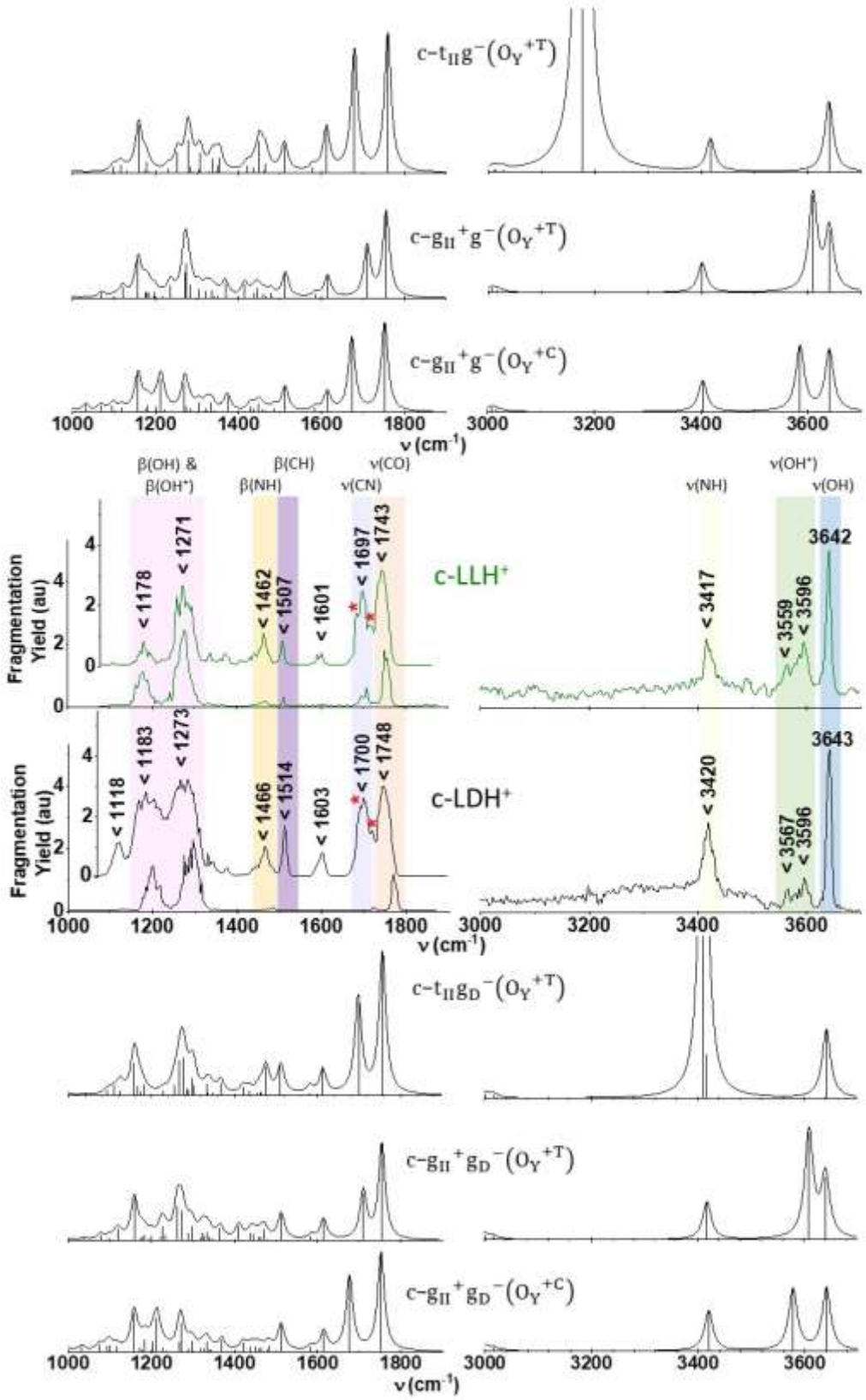

Figure 3. Experimental IRMPD spectra (middle) in the fingerprint region (left) for two laser intensities and in the 3 μm region (right). Simulated IR spectrum of the most stable conformers of c-LLH$^+$ (top) and c-LDH$^+$ (bottom). The bandwidth of the simulated spectra is 10 cm^{-1}.

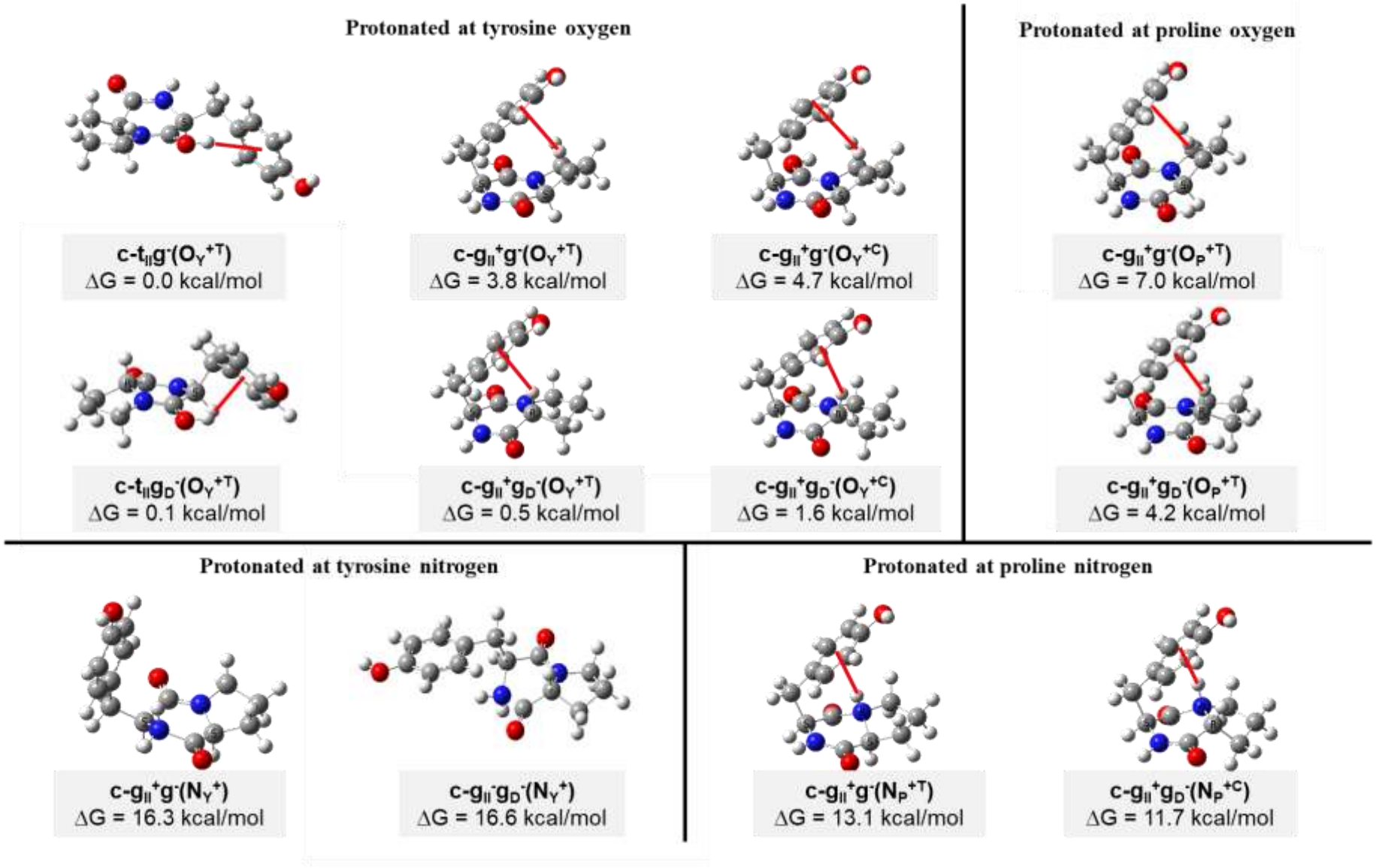

Figure 4. Most stable calculated structures for each protonation site. The hydrogen bonds are indicated by a red line. The Gibbs free energy ΔG is given for each conformer. The zero of the scale is taken at the most stable conformer for each diastereomer. The most stable c-LDH$^+$ conformer is 0.5 kcal/mol above the most stable c-LLH$^+$.

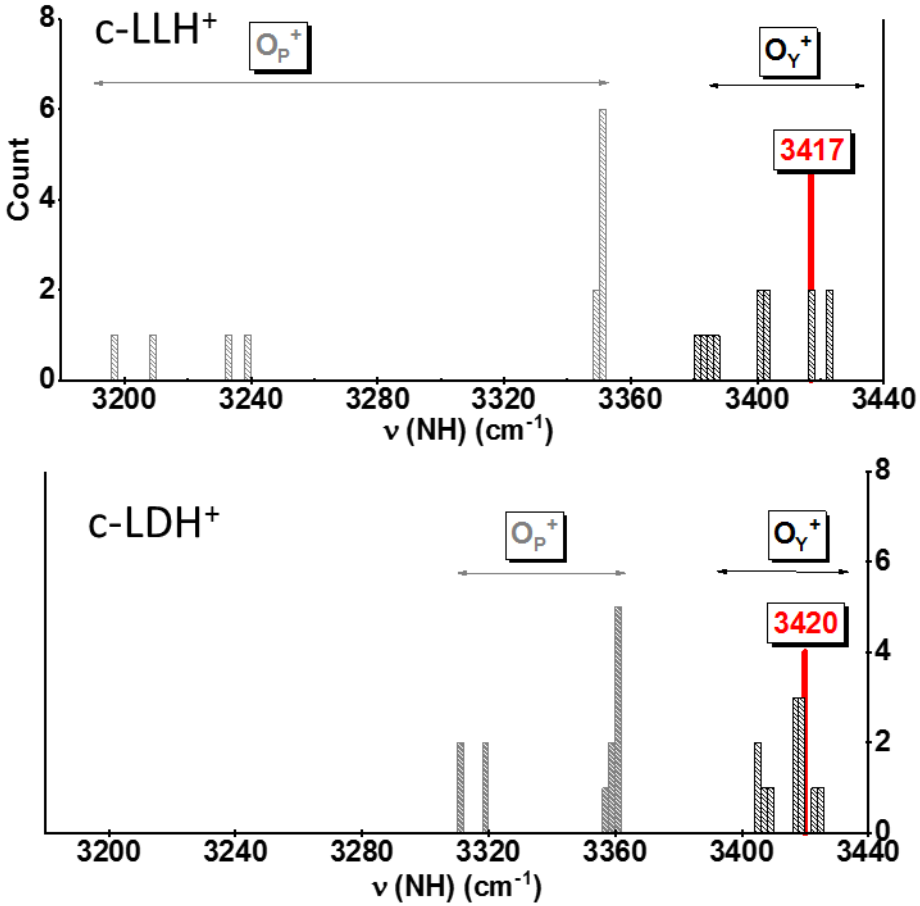

Figure 5. Comparison between the experimental ν(NH) frequencies (red line) and the calculated values for two protonation site, O_P^+ and O_Y^+ (hatched black bars).

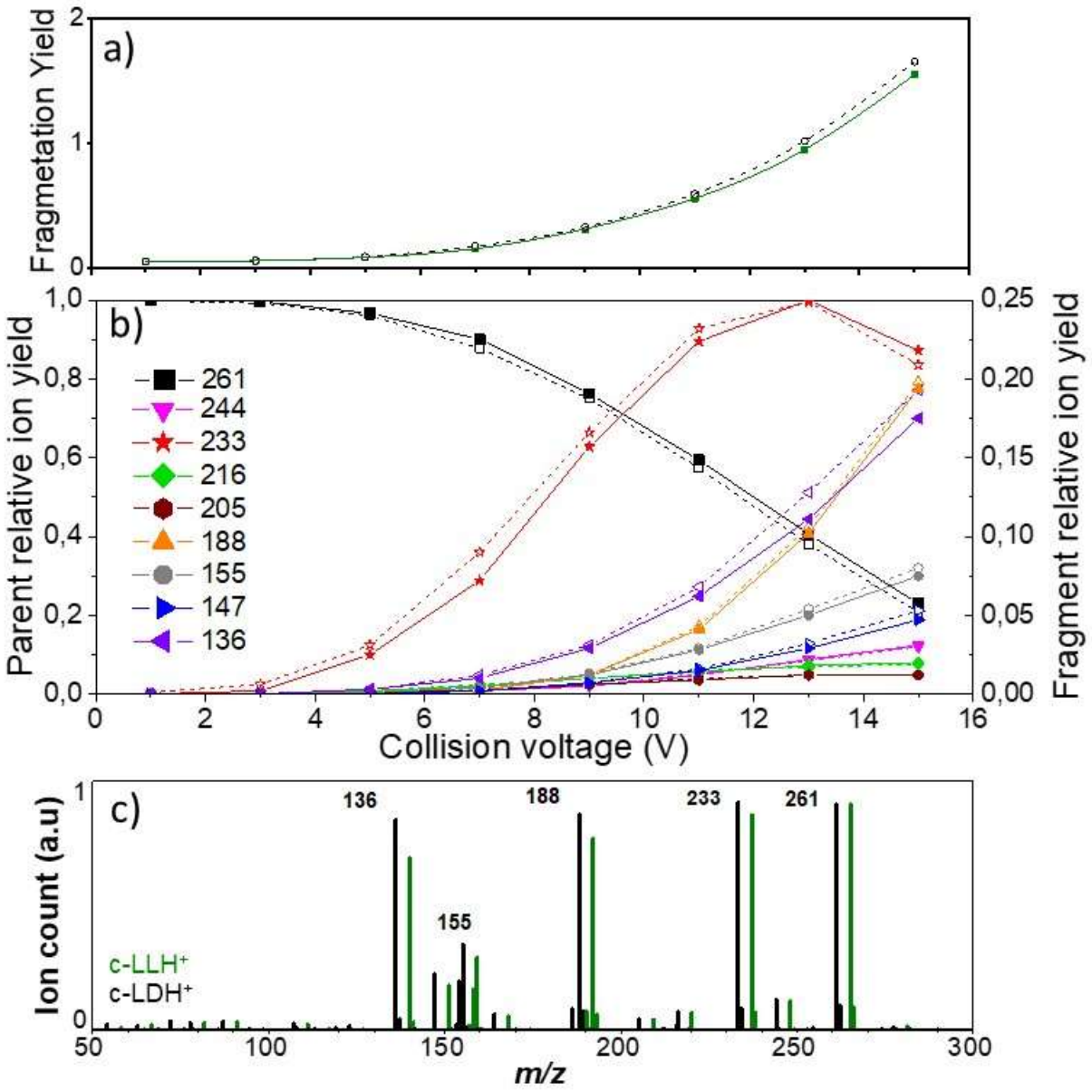

Figure 6. Analysis of the CID-MS^2 spectra of c-LLH^+ and c-LDH^+ as a function of the collision voltage. Continuous lines and filled symbols refer to c-LLH^+ and dashed lines and empty symbols to c-LDH^+.
a) Comparison of the total fragmentation yield of the two diastereomers.
b) Breakdown curve of the parent (*m/z* 261) and main fragments
c) CID-MS^2 spectrum recorded at high collision voltage (15 V). The intensities in both spectra were normalized to that of the parent for better comparison. The spectrum for c-LLH^+ was shifted up by 4 amu for the sake of clarity.

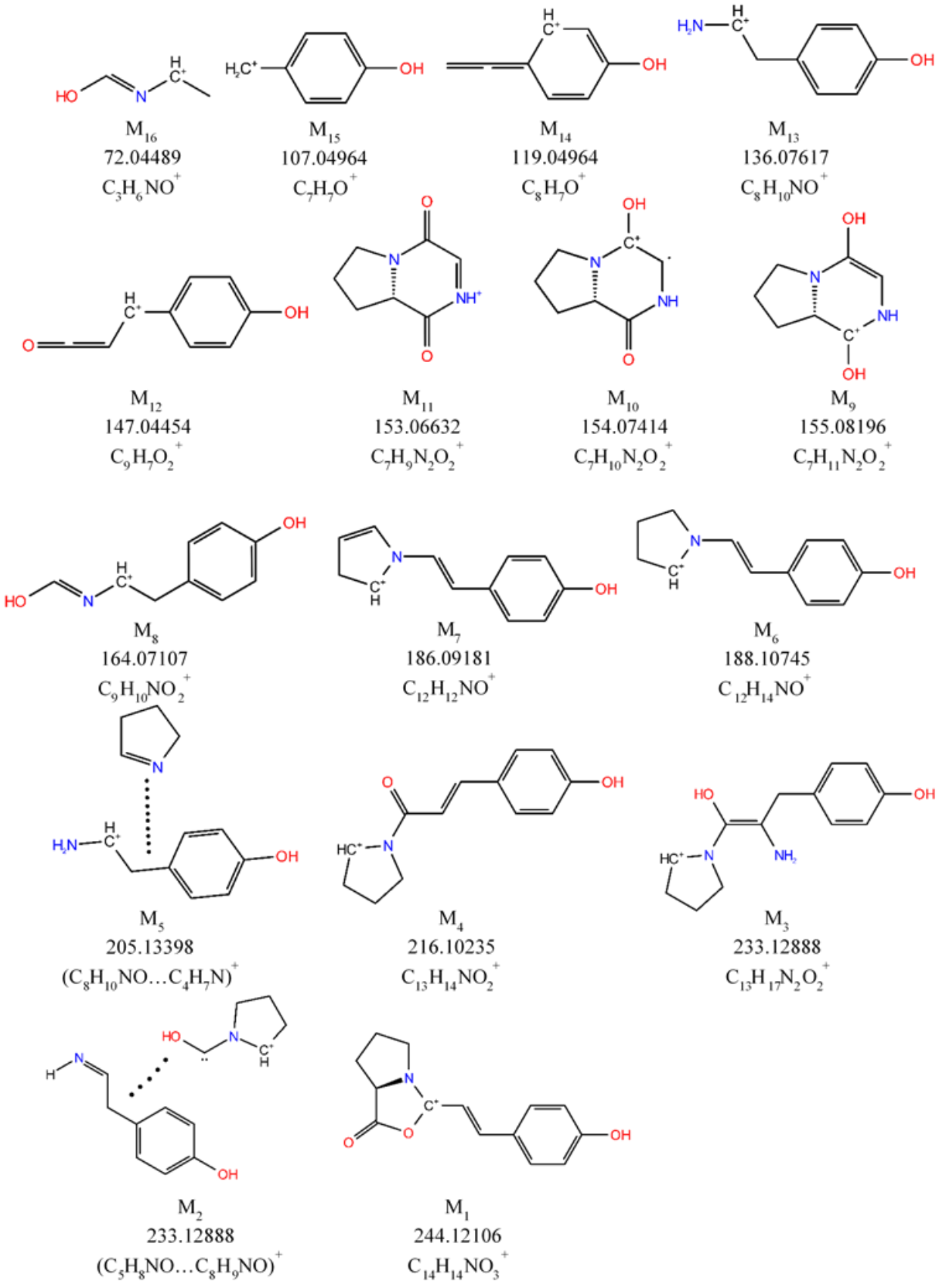

Figure 7: The most abundant isomers of the ionic fragments for each *m/z* and their molecular formula.

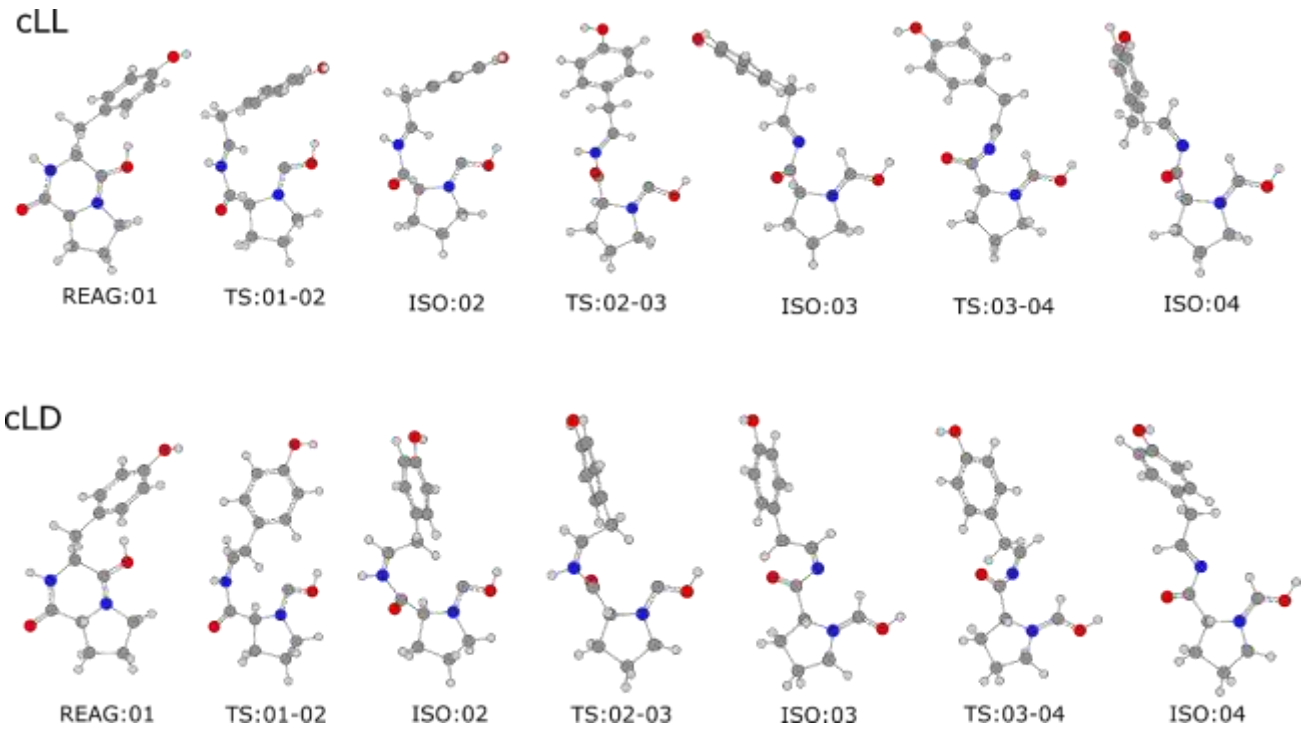

Figure 8: The optimized structure of the reagents (REAG:01), the intermediate states (ISO:02 to :04) occurring during the chemical dynamic simulation, as well as that of the transition states (TS) separating them (see text).

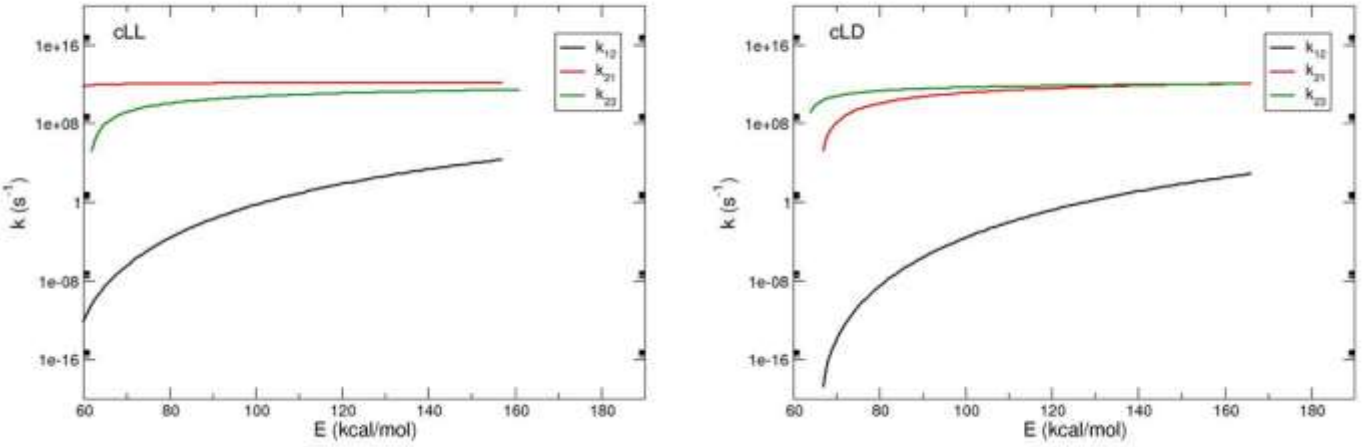

Figure 9. RRKM reaction rate constants as a function of the internal energy for the steps involving REAG:01→ ISO:02 (k_{12}), the corresponding back reaction (k_{21}), and the step involving ISO:02→ ISO:03 (k_{23}) for $cLLH^+$ (left) and $cLDH^+$ (right).

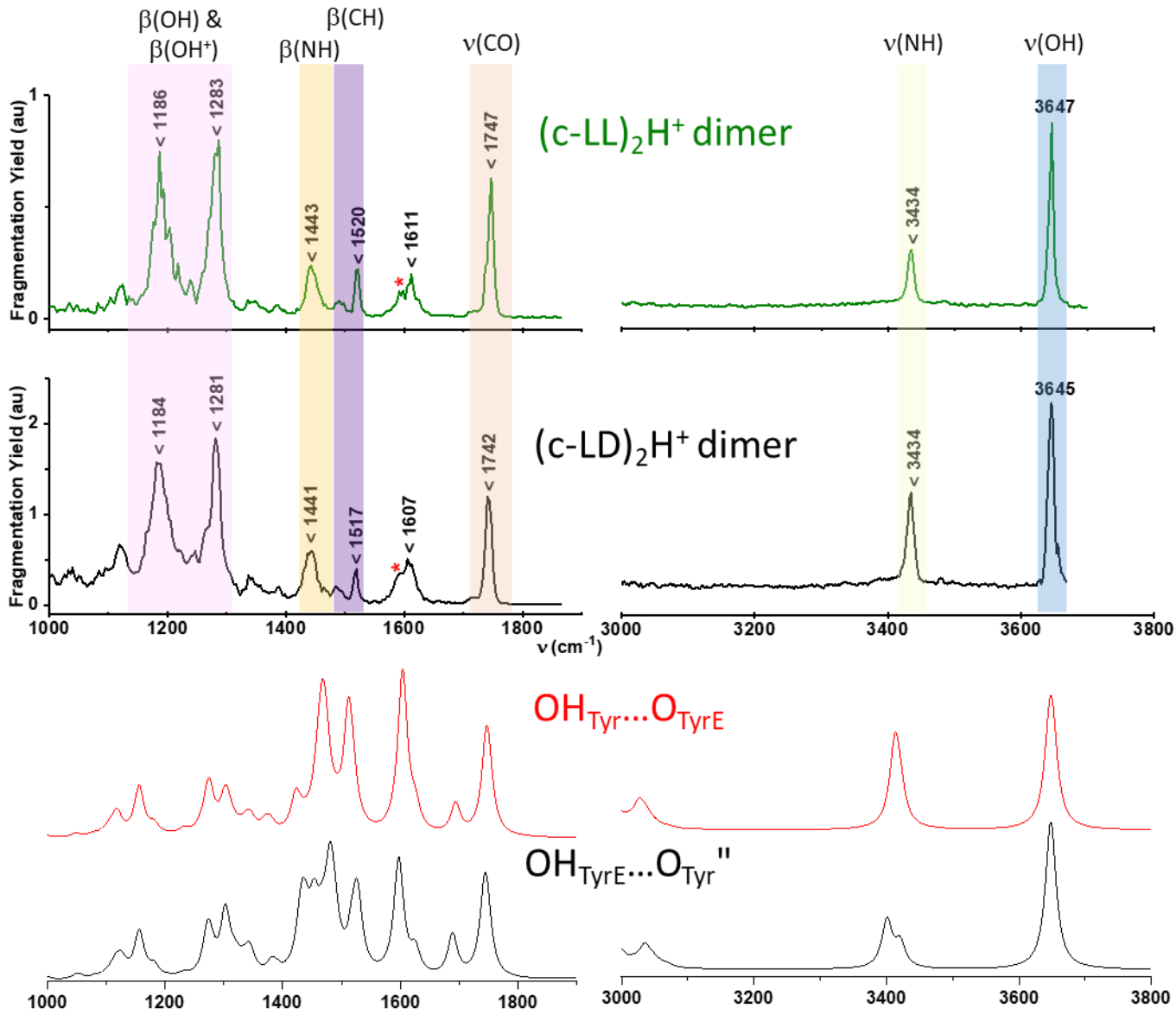

Figure 10. Experimental IRMPD spectra (top) of the protonated dimer of c-LL and c-LD in the fingerprint region (left) and in the 3μm region (right). The different vibrations are highlighted in different colors and labelled. Comparison with calculated spectra (bottom) for $OH_{Tyr}…O_{TyrE}$ and $OH_{TyrE}…O_{Tyr}$".

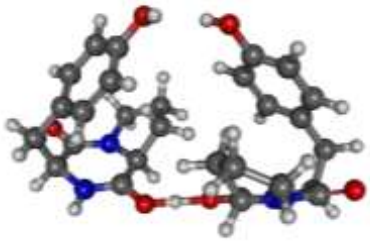

$OH_{Pro}…O_{pro}$
2.1 kcal/mol

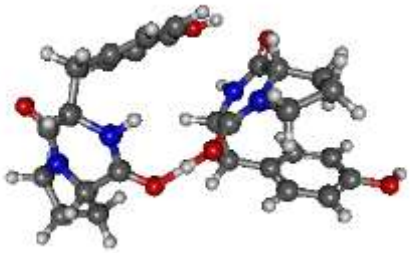

$OH_{Tyr}…O_{pro}$
0.0 kcal/mol

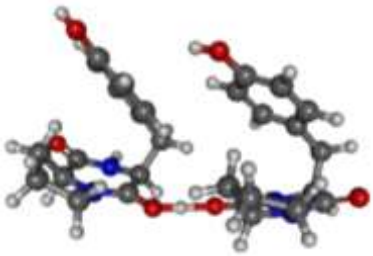

$OH_{Tyr}…O_{Tyr}$
1.1 kcal/mol

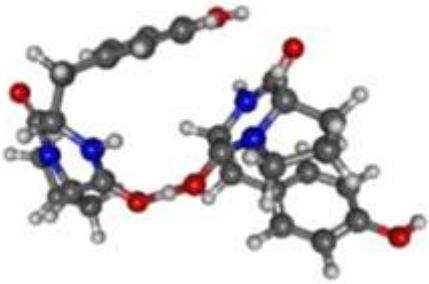

$OH_{Tyr}…O_{Tyr}''$
1.8 kcal/mol

$OH_{Tyr}…O_{TyrE}$
2.0 kcal/mol

$OH_{Tyr}…O_{TyrE}''$
2.7 kcal/mol

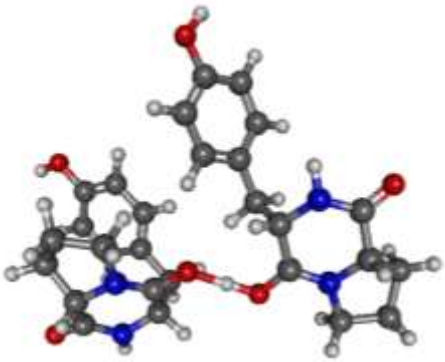

$OH_{TyrE}…O_{tyr}$
3.0 kcal/mol

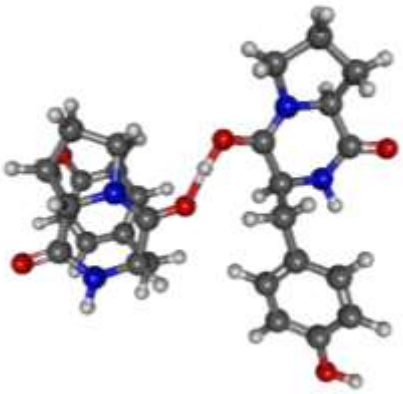

$OH_{TyrE}…O_{Tyr}''$
3.8 kcal/mol

$OH_{TyrE}…O_{TyrE}''$
4.0 kcal/mol

Figure 11. Stable calculated structures of the c-LL protonated dimer with the proton located on one of the amide oxygens. The structures used for the assignment are in bold letters. The relative Gibbs free energy are indicated for each structure.

Stereospecific Collision-Induced Dissociation and Vibrational Spectroscopy of Protonated Cyclo (Tyr-Pro)

Ariel Pérez-Mellor,[a)b)] Ivan Alata,[a)] Valeria Lepere,[a)] Riccardo Spezia,[b)] and Anne Zehnacker-Rentien [a)*1]

a) Université Paris-Saclay, CNRS, Institut des Sciences Moléculaires d'Orsay, 91405, Orsay, France

b) Laboratoire de Chimie Théorique, Sorbonne Université, UMR 7616 CNRS, 4, Place Jussieu, 75005 Paris, France.

Supplementary Information

[1] anne.zehnacker-rentien@universite-paris-saclay.fr

Name	ΔE (kcal/mol)		ΔG (kcal/mol)	
	B3LYP-D3	M06-2X	B3LYP-D3	M06-2X
c-$g_I^+ g^-$ (O_P^{+C})	8.7	7.7	9.2	8.6
c-$g_I^+ g^-$ (O_P^{+T})	6.1	5.0	6.9	6.0
c-$g_I^+ g^-$ (O_Y^{+C})	4.6	3.4	5.3	4.3
c-$g_I^+ g^-$ (O_Y^{+T})	3.7	2.5	4.1	3.7
c-$g_I^- g^-$ (O_P^{+C})	9.5	9.0	9.0	8.7
c-$g_I^- g^-$ (O_P^{+T})	8.4	8.2	7.6	7.7
c-$g_I^- g^-$ (O_Y^{+C})	7.6	7.1	7.3	7.0
c-$g_I^- g^-$ (O_Y^{+T})	5.5	5.1	5.3	5.0
c-$t_{II}\, g^-$ (O_P^{+C})	14.4	13.9	14.0	13.6
c-$t_I\, g^-$ (O_P^{+T})	12.3	11.7	11.8	11.4
c-$t_I\, g^-$ (O_Y^{+C})	9.3	8.6	9.0	8.5
c-$t_I\, g^-$ (O_Y^{+T})	0.1	0.1	0.1	0.0
c-$g_{II}^+ g^-$ (O_P^{+C})	8.9	7.9	9.5	8.8
c-$g_{II}^+ g^-$ (O_P^{+T})	6.3	5.1	7.0	6.1
c-$g_{II}^+ g^-$ (O_Y^{+C})	4.0	2.6	4.7	3.7
c-$g_{II}^+ g^-$ (O_Y^{+T})	3.1	1.8	3.8	3.0
c-$g_{II}^- g^-$ (O_P^{+C})	9.3	8.8	8.9	8.6
c-$g_{II}^- g^-$ (O_P^{+T})	8.3	8.2	7.5	7.6
c-$g_{II}^- g^-$ (O_Y^{+C})	7.7	7.2	7.4	7.1
c-$g_{II}^- g^-$ (O_Y^{+T})	5.6	5.2	5.4	5.1
c-$t_{II}\, g^-$ (O_P^{+C})	14.1	13.6	13.6	13.4
c-$t_{II}\, g^-$ (O_P^{+T})	12.0	11.5	11.5	11.2
c-$t_{II}\, g^-$ (O_Y^{+C})	9.4	8.6	9.0	8.4
c-$t_{II}\, g^-$ (O_Y^{+T})	0.0	0.0	0.0	0.0

Table S1: The relative electronic energy (ΔE) of c-LLH^+ at 0K corrected by the zero-point vibrational energy and the relative Gibbs free energy (ΔG) at standard ambient pressure and temperature (298.15 K, 1 atm) calculated employing two different functionals B3LYP-D3 and M06-2X and the same basis set 6-311++G(d,p).

Name	ΔE (kcal/mol)		ΔG (kcal/mol)	
	B3LYP-D3	M06-2X	B3LYP-D3	M06-2X
c-g_I^+ g_D^- (O_P^{+C})	6.2	6.2	6.7	6.1
c-g_I^+ g_D^- (O_P^{+T})	3.5	3.4	4.0	3.3
c-g_I^+ g_D^- (O_Y^{+C})	1.8	1.7	2.3	1.6
c-g_I^+ g_D^- (O_Y^{+T})	0.7	0.7	1.1	0.5
c-g_I^- g_D^- (O_P^{+C})	9.1	10.0	8.0	8.2
c-g_I^- g_D^- (O_P^{+T})	7.6	8.6	6.6	6.7
c-g_I^- g_D^- (O_Y^{+C})	5.2	6.3	4.5	4.9
c-g_I^- g_D^- (O_Y^{+T})	3.9	5.0	3.1	3.6
c-t_{II} g_D^- (O_P^{+C})	13.6	14.5	12.7	13.0
c-t_I g_D^- (O_P^{+T})	11.3	12.2	10.4	10.6
c-t_I g_D^- (O_Y^{+C})	5.5	5.9	5.0	4.8
c-t_I g_D^- (O_Y^{+T})	0.7	1.5	0.0	0.3
c-g_{II}^+ g_D^- (O_P^{+C})	6.4	6.4	6.8	6.3
c-g_{II}^+ g_D^- (O_P^{+T})	3.7	3.6	4.2	3.5
c-g_{II}^+ g_D^- (O_Y^{+C})	1.1	0.9	1.6	1.0
c-g_{II}^+ g_D^- (O_Y^{+T})	0.0	0.0	0.5	0.0
c-g_{II}^- g_D^- (O_P^{+C})	8.7	9.6	7.7	7.8
c-g_{II}^- g_D^- (O_P^{+T})	7.3	8.3	6.4	6.5
c-g_{II}^- g_D^- (O_Y^{+C})	5.2	6.3	4.6	5.0
c-g_{II}^- g_D^- (O_Y^{+T})	4.0	5.1	3.3	3.8
c-t_{II} g_D^- (O_P^{+C})	13.6	14.6	12.7	13.1
c-t_{II} g_D^- (O_P^{+T})	11.4	12.4	10.5	10.8
c-t_{II} g_D^- (O_Y^{+C})	6.0	6.5	5.4	5.2
c-t_{II} g_D^- (O_Y^{+T})	0.6	1.4	0.1	0.3

Table S2: The relative electronic energy of c-LDH^+ (ΔE) at 0K corrected by the zero-point vibrational energy and the relative Gibbs free energy (ΔG) at standard ambient pressure and temperature (298.15 K, 1 atm) calculated employing two different functionals B3LYP-D3 and M06-2X and the same basis set 6-311++G(d,p).

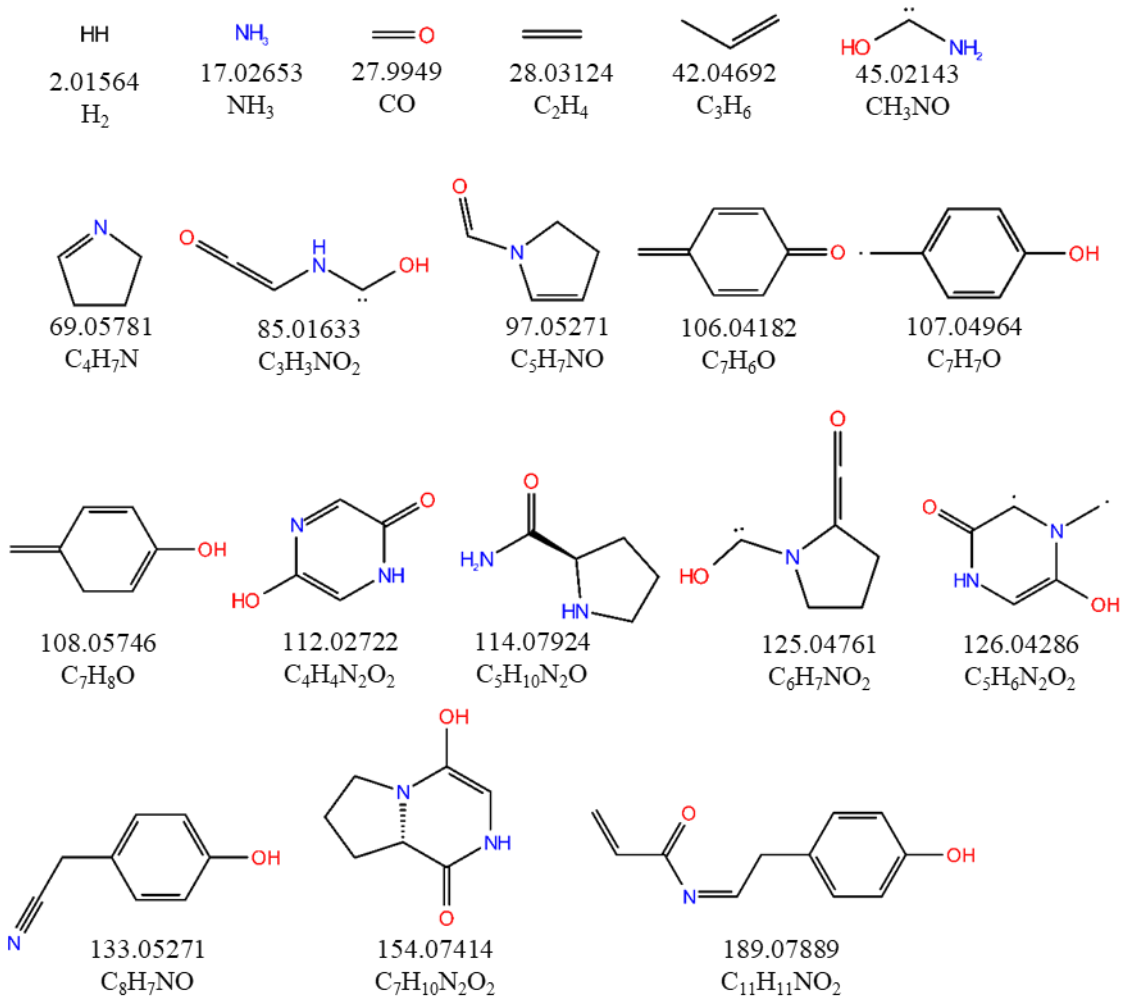

Figure S1: Structure and molecular formula of the most abundant calculated isomers for the neutral fragments.

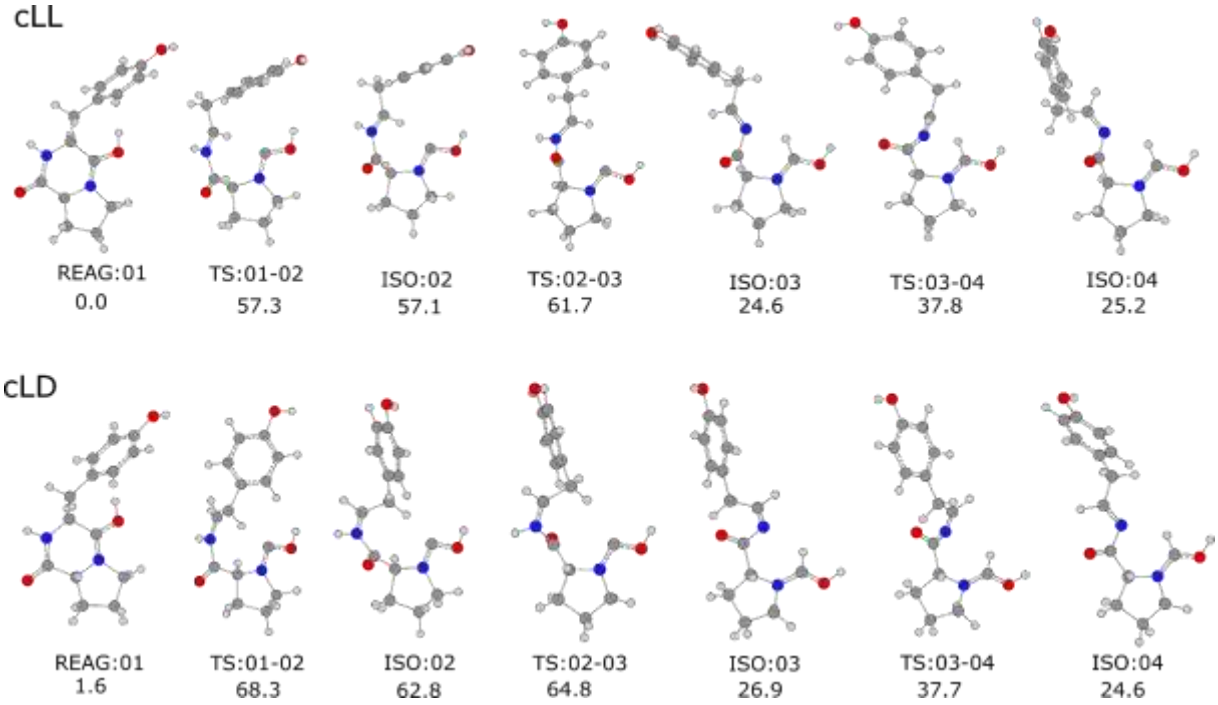

Figure S2: The optimized structure of the reagents (REAG:01), the intermediate states (ISO:02 to :04) occurring during the chemical dynamic simulation, as well as that of the transition states (TS) separating them. The relative ZPE-corrected energy is given for each structure and is calculated at the B3LYP-D3/6-311++g(d,p) level of theory. The values reported are relative to the most stable isomer of the reagent.